

1 Modeling tabular icebergs coupled to an ocean model

2 **A. A. Stern¹, A. Adcroft¹, O. Sergienko¹, G. Marques¹**

3 ¹Geophysical Fluid Dynamics Laboratory, Princeton University
4 ¹201 Forrestal Rd, Princeton, NJ 08540, USA

5 **Key Points:**

- 6 • A novel modeling framework is developed to explicitly model large tabular icebergs
7 submerged in the ocean.
- 8 • Tabular icebergs are represented using Lagrangian elements that drift in the ocean,
9 and are held together by numerical bonds.
- 10 • Breaking the numerical bonds allows us to model iceberg breakup and calving.

11 **Abstract**

12 Large tabular icebergs calved from Antarctic ice shelves have long lifetimes (due to their
 13 large size), during which they drift across large distances, altering ambient ocean circulation,
 14 bottom-water formation, sea-ice formation and biological primary productivity in the
 15 icebergs' vicinity. However, despite their importance, the current generation of ocean cir-
 16 culation models do not represent large tabular icebergs. In this study we develop a novel
 17 framework to model large tabular icebergs submerged in the ocean. In this framework,
 18 tabular icebergs are represented by Lagrangian elements that drift in the ocean, and are
 19 held together and interact with each other via bonds. A break of these bonds allows the
 20 model to emulate calving events (i.e. detachment of a tabular iceberg from an ice shelf)
 21 and tabular icebergs breaking up into smaller pieces. Idealized simulations of a calving
 22 tabular iceberg, its drift, and its breakup, demonstrate capabilities of the developed frame-
 23 work.

24 **1 Introduction**

25 Large tabular icebergs - pieces of floating ice with horizontal dimensions substan-
 26 tially larger than the vertical dimension - calve infrequently (~ every forty-fifty years)
 27 from Antarctic or Greenlandic ice shelves [Jacobs et al, 1992]. Observational estimates
 28 suggest that over the past 30 years approximately half of Antarctic ice-shelf decay is due
 29 to iceberg calving, while the other half occurs through ice-shelf melting [Depoorter et
 30 al, 2013; Rignot et al, 2013]. The infrequently-calved tabular icebergs (horizontal extent
 31 larger than 5 km) account for more than 90% of the Southern Hemisphere iceberg mass
 32 [Tournadre et al, 2016].

33 After calving, icebergs drift away from their origins, often becoming stuck in sea
 34 ice, or grounding on bathymetric highs along the Antarctic coast [Lichy and Hellmer,
 35 2001; Dowdeswell and Bamber, 2007]. Large tabular icebergs extend deep into the water
 36 column, and have the potential to disrupt ocean circulation patterns for months or even
 37 years after calving [Robinson et al, 2012; Stern et al, 2015]. The freshwater flux from
 38 iceberg melt impacts ocean hydrography around the iceberg, influencing sea-ice produc-
 39 tion and bottom-water formation [Arrigo et al, 2002; Robinson et al, 2012; Nicholls et al,
 40 2009; Fogwill et al, 2016]. Because of their large size, the tabular icebergs have long life-
 41 times during which they drift over long distances injecting meltwater along the way and
 42 impacting the Southern Ocean state (e.g. hydrography, sea ice conditions, etc.) far away
 43 from their calving origins [Stern et al, 2016; Rackow et al, 2017]. Meltwater injection
 44 (and the accompanying upwelling) from icebergs can also influence biological productiv-
 45 ity by bringing nutrients to the surface ocean or changing sea ice conditions [Arrigo et al,
 46 2002; Vernet et al, 2012; Biddle et al, 2015]. The increased productivity associated with
 47 free-floating tabular icebergs has been linked with local increases in ocean carbon uptake,
 48 potentially large enough to be a significant fraction of the Southern Ocean carbon seques-
 49 tration [Smith et al, 2007].

50 In recent years, there has been an increased interest in iceberg drift and decay. This
 51 surge of interest has been driven by (i) the need to understand polar freshwater cycles in
 52 order to create realistic climate change and sea level projections [Silva et al, 2006; Shep-
 53 herd and Wingham, 2007; Rignot et al, 2013]; and (ii) the increased navigation and explo-
 54 ration activities in high-latitude iceberg-filled waters in the Arctic [Pizzolato et al, 2012;
 55 Unger, 2014; Henderson and Loe, 2016]. The increased interest in icebergs has led to the
 56 development of numerical models of iceberg drift and decay [Mountain, 1980; Bigg et
 57 al, 1997; Gladstone et al, 2001; Kubat et al, 2005], some of which have been included in
 58 global General Circulation Models [Martin and Adcroft, 2010; Marsh et al, 2015]. These
 59 iceberg drift models treat icebergs as Lagrangian point particles, which are advected by
 60 the flow, and melt according to parameterizations for icebergs melt. Since icebergs are
 61 treated as point particles, iceberg drift models are mostly suitable for modeling icebergs

62 smaller than an ocean grid cell. Consequently, these models have mostly been used to rep-
 63 resent icebergs smaller than 3.5 km on a global scale [Jongma et al, 2009; Martin and
 64 Adcroft, 2010; Marsh et al, 2015].

65 Point-particle iceberg drift models are less suitable for modeling larger tabular ice-
 66 bergs, where the size and structure of the iceberg may be an important feature in deter-
 67 mining their drift and decay [Stern et al, 2016]. They also are not suitable for studying
 68 the local effects that icebergs have on the surrounding ocean, or the small scale processes
 69 that influence iceberg melt and decay [Wagner et al, 2014; Stern et al, 2015]. For these
 70 reasons, tabular icebergs are currently not represented in the iceberg drift models used as
 71 components of climate models, despite accounting for the vast majority of the total South-
 72 ern Hemisphere iceberg mass [Tournadre et al, 2016]. Point-particle iceberg models also
 73 do not have any representation of iceberg breakup and calving, which is known to be an
 74 important iceberg decay mechanism that influences iceberg trajectories.

75 The goal of this study is to develop a new framework to model all kinds of icebergs,
 76 where tabular icebergs are explicitly resolved in the ocean. Our new representation of ice-
 77 bergs aims to include the following key properties: (i) icebergs should be able to travel
 78 large distances within the ocean, (ii) icebergs should melt and decay as they drift in the
 79 ocean, (iii) icebergs should behave as if they have finite extent (in order to study local
 80 effects that icebergs have on the surrounding ocean), and (iv) tabular icebergs should be
 81 able to break away from ice shelves or break into smaller pieces. Properties (i) and (ii)
 82 are common to point-particle icebergs models, while properties (iii) and (iv) are new to
 83 the framework developed in this study. A further requirement of the new framework is
 84 that the model should run sufficiently quickly to be used in general circulation models
 85 used for climate.

86 In order to allow icebergs to travel large distances, we model the icebergs in a La-
 87 grangian framework (as in the point particle iceberg drift models described above). How-
 88 ever in our model icebergs are no longer treated as point particles that interact with the
 89 ocean at a single location. Instead icebergs are given physical structure, so that they inter-
 90 act with the ocean across multiple ocean grid cells, depress the ocean surface over a wide
 91 area, and can interact with other icebergs (Figure 1). This is done by assigning a finite
 92 surface area and shape to the Lagrangian elements, which allows the elements to behave
 93 as if they have a finite extent. The finite extent of an element is transmitted by the ocean
 94 by distributing the element's weight, surface area and melt fluxes over multiple ocean grid
 95 cells in a way which is consistent with the shape of the ice element. Finite-extent ele-
 96 ments interact with each other via repulsive forces which are applied when the boundaries
 97 of the elements overlap. This prevents the icebergs from piling up on top of one another,
 98 which has been an issue near coastlines in previous point-particle icebergs models.

99 Large tabular icebergs can then be represented by ‘bonding’ together multiple ice el-
 100 ements into larger structures using numerical bonds (Figure 1). The numerical bonds hold
 101 the ice elements together and allow a collection of elements to move as a unit. This al-
 102 lows tabular icebergs to drift in the ocean when forced by ocean currents and wind. An
 103 advantage of representing tabular icebergs using numerical bonds is that by breaking the
 104 bonds, we can simulate iceberg calving (e.g.: Figure 2), or the response to an iceberg frac-
 105 turing into multiple smaller pieces (see movies S1 and S2 in the Supporting Information).

106 The manuscript is organized as follows. Section 2 gives a description of the key
 107 aspects of the model developed in this study. Since this model is a new approach to mod-
 108 eling icebergs, we present technical aspects of the model. In Sections 3 and 4, we demon-
 109 strate the capabilities of the model by simulating a tabular iceberg detaching from an ide-
 110 alized ice shelf. In a further simulation we break some numerical bonds within the tabular
 111 iceberg to demonstrate an iceberg splitting in two.

112 **2 Model description**

113 The Kinematic Iceberg Dynamics model (KID) is a Lagrangian particle-based model
 114 in that the objects of the model are Lagrangian elements. Each element represents a col-
 115 umn of ice that is floating in the ocean, and has a position, velocity, mass, and a set of
 116 dimensions, which can evolve in time. The motion of each element is determined by a
 117 momentum equation which is solved in the (Lagrangian) reference frame of the element.
 118 The elements experience oceanic and atmospheric forces, which are either prescribed, or
 119 computed by coupling the iceberg model to an ocean/atmosphere model. The ice elements
 120 also interact with one another via attractive and repulsive interactive forces, and can be
 121 bonded together to form larger structures. The angular momentum of the elements is not
 122 modeled explicitly; instead rotational motion of larger structures emerge as a consequence
 123 of bond orientation and collective motion.

124 In different contexts, the ice elements can be thought to represent individual ice-
 125 bergs, sea ice flows, or, when the elements are bonded together, they can represent larger
 126 structures such as tabular icebergs or ice shelves.

127 The KID model is developed on the code base of an existing iceberg drift model
 128 [Martin and Adcroft, 2010; Stern et al, 2016]. When run with the correct set of runtime
 129 flags, the model runs as a traditional point-particle iceberg drift model.

130 **2.1 Equations of motion**

131 The elements drift in the ocean in response to atmosphere, ocean and sea-ice drag
 132 forces, as well as the Coriolis force, a wave radiation force, a force due to the sea sur-
 133 face slope and interactive forces with other elements. The momentum equation for each
 134 element is given by

$$M \frac{D\vec{u}}{Dt} = \vec{F}_A + \vec{F}_W + \vec{F}_R + \vec{F}_C + \vec{F}_{SS} + \vec{F}_{SI} + \vec{F}_{IA}, \quad (1)$$

135 where $\frac{D}{Dt}$ is the total (Lagrangian) derivative, M is the mass of the element, \vec{u} is the ve-
 136 locity of the element, and the terms on the right hand side give the forces on the element
 137 due to air drag (\vec{F}_A), water drag (\vec{F}_W), sea ice drag (\vec{F}_{SI}), Coriolis force (\vec{F}_C), wave radi-
 138 ation force (\vec{F}_R), sea surface slope (\vec{F}_{SS}), and interactions with other elements (\vec{F}_{IA}).

139 When ice elements move alone (without interactions with other elements), they can
 140 be thought of as representing individual (or clusters of) small icebergs, and follow the
 141 same equations described in the iceberg drift model of Martin and Adcroft [2010] (based
 142 on the equations outlined in Bigg et al [1997] and Gladstone et al [2001]). A description
 143 of these forces is provided for completeness in Appendix A.

144 In addition to the external forces, the ice elements experience interactive forces due
 145 to the presence of other elements. Two types of interactive forces are included between
 146 elements. The first force is a repulsive force which is applied to elements to prevent them
 147 from overlapping the boundaries of the neighboring elements. The second interactive force
 148 is a force due to numerical ‘bonds’, and is only applied if two elements are labelled as
 149 ‘bonded’. When two elements are bonded, each element feels an attractive force that pre-
 150 vents the elements from moving too far apart from one another. The details of the interac-
 151 tive forces are provided in below.

152 **2.2 Interactive Forces**

153 The interactive forces in the model are used to (i) prevent the ice elements from
 154 overlapping and (ii) to connect multiple ice elements together so that the collection of el-
 155 ements moves as a rigid body. Modeling the collisions and movements of rigid objects
 156 precisely, requires very small time steps and precise collision detection algorithms, which

are very computationally expensive. Models using these methods are typically only run for a few days or even a few seconds, and are used to study rapid processes like crack formation or ridging [Hopkins, 2004; Bassis and Jacobs, 2013; Rabatel et al, 2015]). The tabular iceberg framework presented in this study is developed in order to be used in general circulation models used for multi-year simulations. In order to gain the required computational efficiency, we relax the requirement that icebergs must be perfectly rigid and that ice elements can not overlap. Instead, we model the interactive forces between ice elements using damped elastic forces, which can be calculated more efficiently.

The total interactive force on an element is calculated by adding together the interactions with all other elements, such that the interactive force on element i , $(\vec{F}_{IA})_i$ is given by:

$$(\vec{F}_{IA})_i = \sum_{j \neq i} (\vec{F}_{IA})_{ij}, \quad (2)$$

where $(\vec{F}_{IA})_{ij}$ is the force on element i by element j . Both bonded and repulsive interactions are modeled using elastic stresses with frictional damping. The elastic component of the force is a function of the distance between the two elements, while the frictional damping force depends on the relative velocity of the two elements.

To describe the forces between two elements, we begin by introducing some notation. Let \vec{x}_i , \vec{x}_j be the positions of elements i and j . The distance between elements i and j is

$$d_{ij} = |\vec{x}_i - \vec{x}_j|. \quad (3)$$

In calculations of the interactive forces between elements, the elements are assumed to be circular. We define the interaction radius of an element by

$$R_i = \sqrt{\frac{A_i}{\pi}}, \quad (4)$$

where A_i is the planar surface area of element i . Using this, we define the critical-interactive-length scale,

$$L_{ij} = R_i + R_j, \quad (5)$$

which governs interactions between elements i and j . Repulsive forces are only applied when $d_{ij} < L_{ij}$, while for $d_{ij} > L_{ij}$ attractive bonded forces are applied when a bond exists between element i and j (see diagram in Figure 3). The interactive forces are designed such that (in the absence of other external forces) bonded particles will settle in an equilibrium position where elements are separated by L_{ij} .

To aid in notation, we define a bond matrix B_{ij} such that $B_{ij} = 1$ if elements i and j are bonded together and $B_{ij} = 0$ otherwise. Using this notation, the interactive force $(\vec{F}_{IA})_{ij}$ on an element i by an element j is given by

$$(\vec{F}_{IA})_{ij} = \begin{cases} (\vec{F}_e)_{ij} + (\vec{F}_d)_{ij} & \text{if } d_{ij} \leq L_{ij} \\ (\vec{F}_e)_{ij} + (\vec{F}_d)_{ij} & \text{if } d_{ij} > L_{ij} \text{ and } B_{ij} = 1 \\ 0 & \text{if } d_{ij} > L_{ij} \text{ and } B_{ij} = 0 \end{cases} \quad (6)$$

$(\vec{F}_e)_{ij}$ and $(\vec{F}_d)_{ij}$ are the elastic and frictional damping components of the interactive force between elements i and j . The elastic force $(\vec{F}_e)_{ij}$ between elements is given by

$$(\vec{F}_e)_{ij} = -\kappa_e (d_{ij} - L_{ij}) M_{i,j} \vec{r}_{ij}, \quad (7)$$

where $\vec{r}_{ij} = \frac{(\vec{x}_i - \vec{x}_j)}{|\vec{x}_i - \vec{x}_j|}$ is the directional unit vector between the position of element i and j , κ_e is the spring constant, and $M_{i,j}$ is the minimum of the masses of elements i and j . The interactive forces obey Newton's 3rd Law (i.e.: $(\vec{F}_{IA})_{ij} = -(\vec{F}_{IA})_{ji}$). The minimum mass, $M_{i,j}$, is preferred to the average mass, since this means that for two bonded elements a fixed distance apart, the acceleration due to elastic forces is bounded, even when the mass of one of the elements approaches zero.

195 The frictional damping force acts to dampen the relative motion of the two particles.
 196 If \vec{r}_{ij}^\perp is the direction vector perpendicular to \vec{r}_{ij} , and $P_{\vec{r}_{ij}}$ and $P_{\vec{r}_{ij}^\perp}$ are the projection ma-
 197 trices that project onto \vec{r}_{ij} and \vec{r}_{ij}^\perp respectively, then the frictional damping force is given
 198 by

$$(F_d)_{ij} = \left(-c_{r\parallel} P_{\vec{r}_{ij}} - c_{r\perp} P_{\vec{r}_{ij}^\perp} \right) \cdot (\vec{u}_i - \vec{u}_j) \quad (8)$$

199 Here $c_{r\parallel}$ and $c_{r\perp}$ are the drag coefficients for the damping motion parallel and perpen-
 200 dicular to r_{ij} , respectively. We set $c_{r\parallel} = 2\sqrt{\kappa_e}$, so that the elastic force parallel to \vec{r}_{ij} is
 201 critically damped. The perpendicular drag coefficient is set to $c_{r\perp} = \frac{1}{4}c_{r\parallel}$. The perpen-
 202 dicular damping force is used reduce the relative motion of ice elements passing by one
 203 another with overlapping boundaries. The damping forces are implemented using an im-
 204 plicit time stepping scheme, to avoid stability issues for very small elements (details found
 205 in Appendix B).

206 Figure 4 illustrates the effectiveness of the repulsive forces in an uncoupled (ice-
 207 only) simulation. In this simulation ice elements are forced westward into a bay, and
 208 eventually come to rest in the bay with a small amount of overlap between elements. The
 209 amount of overlap between elements in the final state of the simulation depends on the
 210 magnitude of the spring constant, κ_e , with larger spring constants reducing the amount
 211 of overlap. Increasing the spring constant also makes the system numerically stiff so that
 212 smaller time steps are required to prevent numerical instabilities (the system is stable for
 213 time steps satisfying $dt^2 < 4/\kappa_e$). A value of $\kappa_e = 10^{-5}$ is chosen that is large enough to
 214 prevent too much overlap between elements for typical ocean forcings (e.g: Figure 4), and
 215 small enough to allow for time steps up to 10 minutes (smaller time steps are used when
 216 the model is coupled to an ocean model).

217 Figure 5 illustrates the effectiveness of the numerical bonds in simulations of small
 218 icebergs (individual un-bonded elements) and large icebergs (constructed from many ice
 219 elements bonded together) forced to drift towards a convex coast line. When the tabular
 220 icebergs arrive at the coast, they bump into the coastline and begin to rotate, influencing
 221 the paths of the other icebergs. This example illustrates an advantage of using small el-
 222 ements bonded together to represent large-scale structure - i.e. rotational motion of large
 223 structures can be simulated without explicitly accounting for the angular momentum of the
 224 elements (as discussed in Jakobsen [2001]). Movies of these uncoupled simulations are
 225 found in S3 and S4 in the Supporting Information.

226 2.3 Initializing element geometry and packing

227 For purposes of initialization, we assume that elements have surface areas which are
 228 shaped as equally-sized regular hexagons (note that the elements are assumed to be circu-
 229 lar for proposes of interactions). When packing elements together, the hexagonal elements
 230 are initially arranged in a staggered lattice, with each element bonded to the adjacent el-
 231 ements (Figures 1 and 6a). In this arrangement, each element (away from the edges) is
 232 bonded to six other elements. The bonds between elements form a pattern of equilateral
 233 triangles, which gives rigidity to the larger structure. The circular shape of elements (used
 234 for interactions) is inscribed within the hexagonal shape used for packing (Figure 6a). The
 235 centers of adjacent elements are initially separated by a distance $d_{i,j} = L_{i,j} = 2A_p$, where
 236 A_p is the length the apothems of the hexagons.

237 Some experiments were also performed using rectangular elements, arranged in a
 238 regular (non-staggered) lattice. In this case, each element forms four bonds with adjacent
 239 elements. However, the resultant structures were found to be much less rigid and tended
 240 to collapse when sufficient forces was applied. For this reason, we only show the results
 241 using hexagonal elements.

242 2.4 Ocean-ice and ice-ocean coupling

243 The KID model is coupled to the ocean model via a two-way synchronous coupling,
 244 meaning that ocean-model fields are passed to the iceberg model, and iceberg model fields
 245 are passed back to the ocean model at every time step. Passing fields between the two
 246 models involves interpolating the fields from the ocean model's Eulerian grid onto the ice-
 247 berg model's 'Lagrangian grid' (i.e.: onto the ice elements), and aggregating fields from
 248 the Lagrangian elements onto the ocean-model's Eulerian grid.

249 The coupling from the ocean model to the iceberg model is straight forward: at ev-
 250 ery time step: the ocean mixed layer temperature, salinity, velocity and sea-ice concen-
 251 tration are passed from the ocean model to the iceberg model, to be used in the momen-
 252 tum and thermodynamic equations of the ice elements. Since tabular icebergs are explic-
 253 itly resolved in the ocean, it is sufficient for each element to interact with ocean mixed
 254 layer only (i.e.: there is no need to manually embed icebergs into the ocean by integrat-
 255 ing ocean fields over the icebergs' thickness, as suggested in Merino et al [2016]). Within
 256 the KID model, the ocean model fields are interpolated onto the Lagrangian grid using a
 257 bilinear interpolation scheme.

258 The iceberg model influences the ocean by: (i) applying a pressure to the ocean sur-
 259 face, (ii) affecting the upper ocean by applying a no-slip boundary condition and frictional
 260 velocity beneath the ice, and (iii) imposing heat, salt and mass fluxes on the ocean, asso-
 261 ciated with ice melting. Six fields are passed from the iceberg model to the ocean model:
 262 ice mass, ice area, frictional velocity, and heat, salt and mass fluxes. Fields in the iceberg
 263 model are aggregated from the Lagrangian elements to the Eulerian ocean grid before they
 264 are passed to the ocean model.

265 The aggregation of the iceberg-model fields onto the ocean grid is done in a way
 266 that is consistent with the shape of the elements in the iceberg model (see Section 2.3).
 267 Fields are 'spread' to the ocean model grid by exactly calculating what fraction of an el-
 268 ement's surface area lies in a particular grid box, and dividing the field in proportion to
 269 this fraction. As an example, consider a hexagonal element in the iceberg model, which
 270 is positioned such that it intersects four ocean grid cells (Figure 6b). In this situation, the
 271 element's mass (for example) is divided between these four ocean cells in proportion to
 272 the overlap area between the hexagonal element and the grid cell (this fraction is shown
 273 by the colors in Figure 6b). An advantage of this approach is that there are no jumps in
 274 pressure as an element moves from one grid cell to another, which could trigger artificial
 275 tsunamis within the ocean model, making the ocean model unrealistic.

276 The numerical calculation of the intersection between hexagons and the ocean grid
 277 is simplified by dividing the hexagon into 6 equilateral triangles. This method allows for
 278 the intersection to be found even when the hexagon is not aligned with the grid.

279 The aggregation scheme is coded with the restriction that an element's area can only
 280 intersect a maximum of four ocean grid cells at a time. A consequence of this is that this
 281 sets a limit on the maximum size of elements that can be represented using this model,
 282 i.e.: the longest horizontal dimension of an ice element must be smaller than the ocean
 283 grid spacing. Larger ice structures are constructed by bonding together smaller elements.

284 2.5 Melting parameterization

285 The ice elements change their mass and size due to melting, which also affects the
 286 surrounding ocean by changing its heat and salt content. In the model, these processes are
 287 parametrized in several ways. In this section we described the melt parametrization for
 288 bonded, unbonded and partially bonded elements.

289 As mentioned above, ice elements which do not interact with other elements are
 290 modeled identically to the point particle icebergs described in Martin and Adcroft [2010].

These elements melt according to three semi-empirical parametrization for melt commonly used in previous iceberg studies [Gladstone et al, 2001; Martin and Adcroft, 2010]. Three types of iceberg melting are distinguished: basal melt, M_b , melt due to wave erosion, M_e and melt due to buoyant convection, M_v . M_e and M_v are applied to the sides of the ice element, while M_b is applied at the ice element base. The details of M_b , M_v and M_e are given in Appendix A.

When multiple elements are bonded together to form larger structures, it is no longer appropriate to use the melt parameterizations developed for individual point-particle icebergs. An element which is completely surrounded by other elements, is meant to represent a column of ice in the middle of a large structure, and hence will not experience melt at its sides due to wave erosion or buoyant convection. Also, the iceberg basal melt rate, M_b described above is based on boundary layer theory of flow past a finite plate, and is only appropriate for basal surfaces where the distance from the leading edge is sufficiently small [Eckert, 1950; Weeks and Campbell, 1973]. For an element in the interior of a large structure, the distance from the edge of the structure is large, and so using M_b for the basal melt is not appropriate. Instead, the basal melt, M_s is determined using the three equation model for basal melt, which is a typical melting parametrization used beneath ice shelves [Holland and Jenkins, 1999].

When using both individual elements and bonded elements in the same simulation, we determine which melt rate parameterizations to use based on the amount of bonds that each element has. An element in the center of a large structure has the maximum number of bonds, while un-bonded elements has no bonds. If an element can have maximum number of bonds N_{max} , and the number bonds that an element has is N_b , then this element experiences the side melt and bottom melt

$$M_{side} = \frac{(N_{max} - N_b)}{N_{max}} (M_v + M_e) \quad (9)$$

and

$$M_{bottom} = \frac{(N_{max} - N_b)}{N_{max}} M_b + \frac{N_b}{N_{max}} M_s \quad (10)$$

respectively. In this way, elements with no bonds, melt like point-particle icebergs; elements at the center of large structures melt like ice shelves; and elements at the sides of large structures have a combination of iceberg side and basal melt, and ice-shelf melt.

2.6 Algorithms and computational efficiency

Including interactions between elements leads to an increase in the computational complexity of the model. In this subsection we comment on some of the algorithmic procedures that have been used to increase the computational efficiency.

2.6.1 Interactions and Bonds

At every time step, we calculate the force on each element due to interactions with every other element. This involves order N^2 operations (for N elements), which becomes computational expensive as N grows large. We reduce the number of computations by leveraging the fact that each element only has repulsive interactions with elements that are less than one ocean grid cell away, and each element only has bonded interactions with a small number of other elements.

The computation reduction is achieved by storing the element data in an efficient way that eliminates a search through all element pairs to check if they are close to one another or are bonded with one another. The data storage system is organized as follows: pointers to the memory structures containing each element are stored in linked list data structures, which allow elements to be added and removed from the lists easily without restructuring the entire list. Instead of using one list for all the elements on a processor

(as was done in the original code [Martin and Adcroft, 2010]), we use a separate linked list for each ocean grid cell. When an element moves between ocean grid cells, it is removed from its original list and added to the list corresponding to its new ocean grid cell. Since the area of elements has to be smaller than the area of an ocean grid cell, the critical interaction length scale (equation 5) is less than the size of a grid cell. This means that elements only experience repulsive forces with other elements in the same ocean grid cell, or in one of the 8 adjacent cells. At each time step and for each element i , the code traverses the linked lists of the 9 surrounding grid cells, and applies a repulsive force if $d_{i,j} < L_{ij}$ (whether the elements are bonded or not). Limiting the possible repulsive interactions to elements in these 9 linked lists substantially reduces the computational time needed to calculate the total interactive forces.

The attractive forces are computed in a following way. Each bond is assigned a piece of memory. Each ice element contains a linked list of each of its bonds (typically up to six bonds per element). At every time step, the code traverses the lists of bonded elements, and adds an attractive bonded force corresponding to these bonds if $d_{i,j} > L_{ij}$ (the repulsive bonded force to be applied when $d_{i,j} < L_{ij}$ is already accounted for by the procedure outlined in the previous paragraph). Having a list of bonds stored with each element reduces the computations needed for bonded interactions from order N^2 to order N. Computing attractive forces separately from the repulsive forces allows us to avoid checking whether two elements are bonded, which further increases the computational efficiency.

2.6.2 Parallelization and halos

The KID model runs on multiple processors in parallel (using the same grid decomposition as the ocean model). When elements move from an ocean cell on one processor to an ocean cell on a second processor, the memory has to be passed from one processor to the next, added and removed to the appropriate lists and the memory has to be allocated and deallocated correctly. Element interactions across the edge of processors are handled using computational halos. A computational halo is a copy of the edge of a one processor which is appended to the edge of a second processor, so that the first processor can interact with the second processor during a time step. Before each time step, elements at the edges of each processor are copied onto the halos of adjacent processors so that they can be used in calculating the interactive forces. After each time step, these halos are emptied, and the process is repeated. These halo updates are one of the most computationally expensive parts of the iceberg model. Details of how the bonds are broken and reconnected across processor boundaries are provided in Appendix C.

2.6.3 Time stepping

The elements in the iceberg model are advected using a semi-implicit velocity Verlet time-stepping scheme. The velocity Verlet time stepping scheme is commonly used in discrete element models in video games because it is computational efficient and has desirable stability properties [Jakobsen, 2001]. This time stepping scheme was preferred to the Runge-Kutta 4, which was used in the iceberg model of Martin and Adcroft [2010] since the Verlet time stepping only requires one calculation of the interactive forces once per time step (while the Runge-Kutta scheme requires the interactive forces to be calculated four times). Since the calculation of the interactive forces is one of the most computationally expensive part of the algorithm, the Verlet scheme leads to a significant increase in the computational efficiency of the model. The Verlet scheme used in the model contains a modification of the original (fully explicit) velocity Verlet time stepping scheme in that damping terms are treated implicitly (which increases the numerical stability). The details of this adapted time stepping schemed are outlined in Appendix B.

3 Experiment Setup

The introduction of Lagrangian elements, numerical bonds and interpolation schemes between the Eulerian and Lagrangian grids (discussed in Section 2) means that we now have the tools to model large tabular icebergs submerged in the ocean. We demonstrate this capability by simulating a tabular iceberg drifting away from an ice shelf in idealized setting.

3.1 Model configuration

We use the geometric setup of the Marine Ice Ocean Modeling Inter-comparison Project (MISOMIP) [Asay-Davis et al, 2016]. The configuration consists of an idealized ice shelf in a rectangular domain. The domain is $L_x = 80$ km wide and $L_y = 480$ km long, and contains an ice shelf which is grounded on the south side of the domain and has an ice front at $y=650$ km. The ice thickness and bottom topography of this setup are shown in Figure 7a and 7c respectively, with the grounding line position drawn in for reference. The configuration is the same as that of the Ocean0 setup in the MISOMIP, with a few minor changes to the ice-shelf geometry (see the Supporting Information for details).

3.2 Initializing Lagrangian elements:

The idealized ice shelf is constructed out of Lagrangian ice elements. Ice elements are hexagonal and are arranged in a regular staggered lattice (as discussed in Section 2.3). The sides of the hexagons are initialized with length $S = 0.98$ km. Gaps along the boundaries are filled in using smaller elements so that the total ice-shelf area is preserved. The initial mass of the ice elements is determined by a preprocessing inversion performed before the model is run. When the model runs, the mass of elements is aggregated from the Lagrangian grid onto the Eulerian ocean grid (see Section 2.3), and is used to find the surface pressure and ice draft (part of an ice column submerged into the ocean). The ice draft calculated without the aggregation (treating elements as point masses) contains large grid artifacts (Figures 7b). These grid artifacts are much reduced after the mass-spreading aggregation is used (Figure 7c).

3.3 Ocean model setup

The iceberg model is coupled to the MOM6 ocean model [Hallberg et al, 2013]. The ocean model configuration uses a vertical coordinate system which is a hybrid between a sigma-level and a z-level coordinate. In particular, model layers deform underneath the ice shelf as they would in a sigma-coordinate model, but collapse to zero thickness when they intersect with bottom topography, as they would in a z-level model. The coordinate system was achieved using ALE regridding-remapping scheme [White et al, 2009]. The model uses a horizontal resolution of 2 km, and 72 vertical layers. All simulations were repeated using the ocean model configured in isopycnal mode (results were similar and are not presented here).

Ocean parameters are as specified in the MISOMIP configuration [Asay-Davis et al, 2016], and are shown in Table 1. The simulation is initially at rest, with horizontally uniform initial ocean temperature and salinity profiles which vary linearly between specified surface and bottom values: $T_{top} = -1.9^\circ \text{C}$, $T_{bottom} = 1.0^\circ \text{C}$, $S_{top} = 33.8 \text{ psu}$, $S_{bottom} = 34.7 \text{ psu}$. The maximum ocean depth is $H_{ocean} = 720 \text{ m}$. A sponge layer is used on the northern boundary of the domain, which relaxes the temperature and salinity back to the initial temperature and salinity profile. The sponge layer has length $L_{sponge} = 10 \text{ km}$, and has a relaxation time scale parameter $T_{sponge} = 0.1 \text{ days}$ at the northern boundary. The inverse of the relaxation time scale parameter drops linearly to zero over the length of the sponge layer. Melting is set to zero for ocean cells where the ocean col-

umn thickness is less than 10m to avoid using more energy to melt ice than is present in the water column.

3.4 Spinup period:

The model is spun-up for 5 years with all ice elements being fixed. During spinup, the injection of buoyant meltwater at the base of the ice shelf drives a clockwise circulation within the domain (not shown). The circulation compares well with an identical static ice-shelf experiment run using an Eulerian ice shelf model [Goldberg et al, 2012]. A detailed comparison of the Lagrangian and Eulerian ice shelf models is presented in a separate study, and is not shown here.

3.5 Iceberg calving:

After spinup, a large tabular iceberg detaches from the ice shelf, and is allowed to drift into the open ocean. This is achieved by allowing all ice elements initially within a 14.4 km radius of the center of the ice front to move freely while the other ice elements continue to be held stationary. Ice elements less than 12 km from the center of the ice front, are bonded together to form a semi-circular tabular iceberg. A ring of elements whose distance, d , from the ice front center obeys $12 \text{ km} \leq d \leq 14.4 \text{ km}$, are allowed to move freely, but have all their bonds removed. Elements in this half annulus represent fragments of the ice shelf which calve into small pieces during the calving event.

After the spinup period, a wind stress $\vec{\tau} = <\tau_x, \tau_y> = <0.05, 0.05> \frac{N}{m^2}$ is applied to drive the tabular iceberg away from the ice-shelf cavity. This is referred to as the Control simulation. Perturbation experiments were also performed using other wind stress values. Further perturbation experiments were performed by breaking some numerical bonds in order to break the tabular iceberg into smaller pieces.

4 Model Results

After spinup of the Control simulation, the elements near the ice-shelf front are allowed to move freely, and the icebergs begin to drift away from the ice shelf while fully submerged in the ocean (see Figures 2 and 8, and the movie S1 in the Supporting Information). At this point, the iceberg model and the ocean model are fully coupled: changes to the iceberg position alter the top-of-ocean pressure and dynamical boundary condition; and changes to the iceberg melt rates alter the top-of-ocean temperature, salt and mass fluxes. These changing ocean boundary conditions influence the ocean by triggering gravity waves, driving surface mixing, and affecting the ocean stratification. The evolving ocean velocities, temperatures and salinities feedback onto the ice elements by changing the force balance on the ice elements (leading to changes in the elements' position), and altering the melt rates. The various feedbacks within this coupled system offer many opportunities for the model to become unstable. The fact that the model is stable and that we are able to simulate tabular icebergs moving in the ocean without the modeling crashing and introducing artificial effects like tsunamis, is a non-trivial technical milestone.

4.1 Iceberg motion

In the Control simulation, the semi-circular tabular iceberg moves as a cohesive unit due to the presence of the numerical bonds, while the smaller ice fragments quickly disperse (Figure 2). The tabular iceberg drifts towards the north east, driven by the wind and steered by the Coriolis force. As the tabular iceberg drifts northwards, it rotates in a counterclockwise direction (the direction of the Coriolis force in the Southern Hemisphere), and makes contact with the eastern boundary of the domain, before continuing northward.

477 Most of the smaller ice fragments also move to the northeast, but not as a cohesive unit.
 478 Some of these element also move to other parts of the domain.

479 The direction (and speed) of the iceberg drift is largely determined by the wind
 480 speed and direction. Perturbation experiments using different wind stresses show that for
 481 sufficiently large winds, the tabular iceberg drifts to the north east when $\tau_x > 0$, and to the
 482 north west when $\tau_x < 0$ (not shown). For a purely zonal wind stress with $|\tau_x| \leq 0.01 \frac{N}{m^2}$,
 483 the iceberg does not move away from the ice shelf. When the wind is purely offshore
 484 ($\tau_x = 0.0 \frac{N}{m^2}$), a meridional wind stress $\tau_y \geq 0.05 \frac{N}{m^2}$ is needed to move the tabular ice-
 485 berg away from the ice shelf. While this result is partly an artifact of the chosen shape
 486 of the calving iceberg, it is also consistent with Bassis and Jacobs [2013] who noted that
 487 calving is a two step process consisting of (i) ice-shelf rifting that forms an iceberg and
 488 (ii) iceberg detachment. The results here suggest that strong (cross-shore) winds may be
 489 required to drive large tabular icebergs away from their source ice shelves.

490 4.2 Breaking bonds

491 The numerical bonds in the KID model enable the tabular iceberg to retain its shape.
 492 This is demonstrated by comparing the Control simulation to an identical simulation where
 493 all numerical bonds have been removed (Figure 9, movie S5). In the bond-free simula-
 494 tion, the ice elements disperse and the calved iceberg quickly loses its original structure.
 495 This bond-free simulation does not adequately represent tabular iceberg, which can move
 496 long distances through the ocean as a cohesive unit. This result motivates the inclusion of
 497 bonds in the iceberg model, even though they are more computationally expensive than
 498 traditional point-iceberg models.

499 By breaking some (but not all) numerical bonds, we can simulate breaking of tab-
 500 ular icebergs into smaller pieces. Figure 10 shows the results of an experiment which
 501 is identical to the Control experiment, except that all numerical bonds that intersect the
 502 line $x = \frac{L_x}{2}$ have also been severed. This effectively cuts the large tabular iceberg into
 503 two halves. As the icebergs drift northwards, the two halves of the tabular iceberg each
 504 move as a cohesive unit, but they are able to move independently of one other (Figure 10,
 505 movie S2). The two large fragments initially move together, but begin to separate after
 506 a few days. The breaking of a tabular iceberg has the additional effect of increasing the
 507 total surface area of ice exposed to the ocean, thus increasing the total decay rate of the
 508 icebergs.

509 4.3 Ocean response

510 Since the tabular iceberg is submerged in the ocean, the iceberg calving and drift af-
 511 fects the surrounding ocean. In the Control simulation, as the tabular iceberg drifts north-
 512 ward a warming of the surface waters is observed around the tabular iceberg, with the
 513 largest warming occurring at the ice-shelf front and along the tabular iceberg's rounded
 514 edge (Figure 2). This surface warming is caused by upwelling of the warmer waters from
 515 beneath the ice shelf and iceberg. As the icebergs drifts away from the ice shelf, these
 516 warmer waters remain at the surface, mapping out the iceberg wake (Figure 2). The mo-
 517 tion of the tabular iceberg disturbs the ocean surface, which affects ocean velocities through
 518 out the water column (Figure 11). The elevated shears around the tabular iceberg lead to
 519 increased vertical mixing in the vicinity of the iceberg, which alters the stratification of
 520 the water column (Figure 8), warming the upper ocean. The signature of upwelling wa-
 521 ter in the wake of a drifting tabular iceberg bears some similarity to satellite observations
 522 of streaks of increased ocean color in the wake of tabular iceberg in the Southern Ocean
 523 [Duprat et al, 2016], suggesting that the increased productivity around icebergs may be
 524 driven by upwelling water delivering nutrients to the surface.

525 **4.4 Iceberg melt rates**

526 The increased subsurface velocities and temperatures cause elevated melt rates at
 527 the base of the ice shelf and iceberg (Figure 12). The largest melt rates are observed at
 528 the newly calved ice-shelf front and on the rounded side of the tabular iceberg (Figure
 529 12a), where the iceberg calving has created steep ice cliffs. These sharp ice fronts allow
 530 for large ocean currents (Figure 12c), which drive the elevated melt rates. The elevated
 531 melt rates act to smooth out the ice front over time, making the ice cliff less steep. While
 532 this is likely a real phenomena that could be observed in nature, we should be wary of the
 533 modeled velocities at the ice cliffs, since large changes in ice thicknesses are associated
 534 with numerical pressure gradient errors which can drive spurious motion.

535 The large melt rates along the ice edges are also partly driven by the fact that dif-
 536 ferent melt parametrization are used in the interior and edges of large ice structures (see
 537 Section 2.5). Figure 13 shows the melt rates computed with (a) the 3-equation-model
 538 parametrization [Holland and Jenkins, 1999], (b) point-particle-iceberg-melt parametriza-
 539 tion [Gladstone et al, 2001], and (c) the mixed-melt-rate parametrization (introduced in
 540 Section 2.5). The 3-equation-model melt rates (Figure 13a) are less than a third of the
 541 size of those calculated using the point-particle-iceberg-melt parametrization (Figure 13b).
 542 When the mixed-melt-rate parametrization is used (Figure 13c), the very high melt rates
 543 are only observed at the edges of ice structures.

544 **5 Summary**

545 In this study we present a novel framework for simulating tabular icebergs in ocean
 546 models, and representing icebergs with finite extent and structure. In this framework, large
 547 tabular icebergs are represented by collections of Lagrangian elements that are held to-
 548 gether by numerical bonds. Each ice element is assigned a surface area and shape, and
 549 can interact with the ocean and other elements in a way which is consistent with the shape
 550 of the element. Such a representation allows tabular icebergs to interact with the ocean
 551 across a wide area (larger than a grid cell), and individual ice elements to behave as if
 552 they had a finite extent. This is in contrast to previous representations of icebergs in nu-
 553 merical models [Jongma et al, 2009; Martin and Adcroft, 2010; Marsh et al, 2015] that
 554 treat icebergs as point particles. Assigning a finite extent to elements prevents icebergs
 555 from piling up on top of one another, which has been an issue for previous point-particle
 556 iceberg models. Explicitly resolving tabular icebergs in the ocean allows the icebergs to
 557 interact with the ocean in a more realistic way, and allows us to study the effects that tab-
 558 ular icebergs have on ocean circulation. Including numerical bonds between elements al-
 559 lows for simulations which emulate iceberg calving and fracture by severing the bonds.

560 The capabilities of the tabular iceberg model are demonstrated by modeling a tab-
 561 ular iceberg drifting away from an idealized ice shelf (also constructed using Lagrangian
 562 elements). The results show that explicitly resolving tabular icebergs in the ocean allows
 563 for a complex interaction between the iceberg and the surrounding ocean. In our Con-
 564 trol setup, a tabular iceberg is driven away from the ice shelf by ocean currents, wind
 565 stress, and the Coriolis force. As the iceberg moves through the water, it disturbs the
 566 ocean surface, driving ocean currents. The motion of the iceberg and melt beneath the
 567 iceberg drive upwelling along the sides of the iceberg, which entrains ambient water and
 568 causes a warming of the surface ocean in the wake of the iceberg. The changing ocean
 569 conditions feed back onto the iceberg, affecting its motion and melt rates. The highest
 570 melt rates are observed at edge of the iceberg which has the steepest ice cliff. These have
 571 the effect of smoothing out the ice edge over time. Simulations without using numerical
 572 bonds showed that the bonds are essential for allowing the iceberg to move as a unit. We
 573 also demonstrate that by breaking these numerical bonds we can simulate iceberg fracture,
 574 which is important process that increases the rate of iceberg decay.

To our knowledge, the model presented in this study is the first model to explicitly resolve drifting tabular icebergs in an ocean model that can be used for climate studies. A natural extension of this work is a representation of tabular icebergs in a general circulation model (GCM). However, before this can be done, there are a number of issues that need to be resolved: firstly, the question of how and when to introduce tabular icebergs into the ocean needs to be addressed. For GCM's with active ice shelves, a calving law is needed to release the tabular iceberg into the ocean. The question of what calving law to use is a topic of ongoing research [Benn et all, 2007; Alley et al, 2008; Levermann et al, 2012; Bassis and Jacobs, 2013] and is still unresolved. One potential way to temporarily bypass this problem would be to run hindcast simulations using historically observed calving events. A related issue is the question of how and when to break the bonds within the freely floating icebergs to simulate iceberg breakup. Without a rule for iceberg breakup, the tabular icebergs would likely drift to unrealistically low latitudes. Further work is also needed to understand (and model) the interactions between tabular icebergs and sea ice, and to parametrize the effects of iceberg grounding, as these interactions play a large role in dictating the trajectories of tabular icebergs. However, despite these remaining challenges, the technical framework described in this article is potentially a useful step towards including tabular icebergs in global GCM's.

6 Appendix A

6.1 Environmental forces on ice elements

The non-interactive forces on an ice element are as described in [Martin and Adcroft, 2010], and are repeated here for completeness. The forces on an element due to air (a), ocean (o) and sea ice (si) drag are given by

$$\vec{F}_a = \rho_a (0.5c_{a,v}WF + c_{a,h}LW)|\vec{u}_a - \vec{u}|(\vec{u}_a - \vec{u}), \quad (11)$$

$$\vec{F}_o = \rho_o (0.5c_{o,v}W(D - T_{si})F + c_{o,h}LW)|\vec{u}_o - \vec{u}|(\vec{u}_o - \vec{u}), \quad (12)$$

$$\vec{F}_{si} = \rho_{si} (0.5c_{si,v}WT_{si}F + c_{si,h}LW)|\vec{u}_{si} - \vec{u}|(\vec{u}_{si} - \vec{u}). \quad (13)$$

Here ρ_a , ρ_o , ρ_{si} , are the density of air, ocean and sea ice, respectively. $c_{a,v}$, $c_{o,v}$ and $c_{si,v}$ are the vertical drag coefficients with air, ocean and sea ice, while $c_{a,h}$, $c_{o,h}$ and $c_{si,h}$ are the respective horizontal drag coefficients. \vec{u}_a , \vec{u}_o , \vec{u}_{si} , are the velocities air, ocean and sea ice, respectively. L, W, T, F and D are the length, width, thickness, free-board and draft of the ice element. The element thickness is related to the draft and free-board by $T = F + D$ and $D = \frac{\rho}{\rho_o}T$, where ρ is the ice element density. T_{si} is the sea ice thickness.

The wave radiation force (\vec{F}_R) is given by

$$\vec{F}_R = \frac{1}{2}\rho_o c_r g a \min(a, F) 2 \frac{WL}{W + L} \frac{\vec{v}_a}{|\vec{v}_a|} \quad (14)$$

where g is the acceleration due to gravity, a is the wave amplitude empirically related to the wind speed by $a = 0.010125|\vec{v}_a - \vec{v}_o|$, and c_{wd} is the wave drag coefficient defined as

$$c_{wd} = 0.06 \min \left(\max \left[0, \frac{L - L_c}{L_t - L_c} \right], 1 \right), \quad (15)$$

where $L_w = 0.32|\vec{v}_a - \vec{v}_o|^2$ is an empirical wave length, $L_c = 0.125L_w$ is the cutoff length, and $L_t = 0.25L_w$ is the upper limit.

The pressure gradient force is approximated as a force due to sea surface slope and given by

$$\vec{F}_{SS} = -Mg \vec{\nabla} \eta \quad (16)$$

where η is the sea surface height.

615 6.2 Melt rate parametrization

616 As discussed in Section 2.5, unbounded ice elements in the KID decay according to
 617 parameterizations for iceberg decay typically used in iceberg drift models [Martin and Ad-
 618 croft, 2010], while ice elements within larger ice structures have only a basal melt given
 619 by the three equation model [Holland and Jenkins, 1999].

620 For unbonded ice elements, the element thickness decays due to basal melt at a rate
 621 M_b , while the length and width of the elements decay as a result of melt due to wave ero-
 622 sion, M_e , and melt due to buoyant convection, M_v . Following Gladstone et al [2001] and
 623 Martin and Adcroft [2010], the basal melt rate, wave erosion melt rate, and buoyant con-
 624 vention melt rate are parameterized by

$$625 M_b = 0.58|\vec{v} - \vec{v}_0|^{0.8} \frac{\tilde{T}_0 - \tilde{T}}{L^{0.2}} \quad (17)$$

$$626 M_e = \frac{1}{12} S_s \left(1 + \cos [\pi A_i^3]\right) \left(\tilde{T}_0 + 2\right), \quad (18)$$

$$627 M_v = \left(7.62 \times 10^{-3}\right) \tilde{T}_0 + \left(1.29 \times 10^{-3}\right) \tilde{T}_0^2. \quad (19)$$

628 \tilde{T} is the effective iceberg temperature and is set to $\tilde{T} = 4^\circ\text{C}$, \tilde{T}_0 is the temperature at the
 629 top of the ocean, A_i is the sea-ice area fraction, and S_s is the sea state, which is given by
 the Beaufort scale

$$630 S_s = \frac{2}{3} |\vec{u}_a - \vec{u}_o|^{\frac{1}{2}} + \frac{1}{10} |\vec{u}_a - \vec{u}_o| \quad (20)$$

All three melt rates are in units of meters per day.

631 For elements inside larger structures, the melt due to wave erosion and melt due to
 632 buoyant convection are set to zero, and the basal melt, M_s , is given by the standard three
 633 equation model [Holland and Jenkins, 1999].

634 7 Appendix B

635 7.1 Modified Verlet Algorithm

636 The KID uses a version velocity Verlet time-stepping algorithm, which has been
 637 modified to allow part of the forcing to be calculated implicitly. The traditional velocity
 638 Verlet algorithm is commonly used in molecular dynamics, as it is simple to implement,
 639 second order accurate and computationally efficient [Swope et al, 1982; Omelyan et al,
 640 2002]. Here we modify the traditional scheme to allow for the drag forces to be modeled
 641 implicitly, which prevents large accelerations for element's whose mass approaches zero.
 642 To do this, we include both an implicit and explicit acceleration, $a = a^{exp} + a^{imp}$. The
 643 explicit acceleration, a^{exp} , includes all forcing terms which depend only on the previous
 644 time step and the current position, while the implicit acceleration, a^{imp} , includes forcing
 645 terms which depend on the velocity at the current time step (in particular the drag and
 646 Coriolis forces).

647 Using a time step of Δt , and subscripts to denote the time step (so that $t_{n+1} = t_n +$
 648 Δt), the modified velocity Verlet scheme can be written as:

- 649 1) Calculate updated position: $x_{n+1} = x_n + u_n \Delta t + \frac{1}{2} \Delta t^2 \left(a_n^{exp} + a_n^{imp}\right).$
- 650 2) Calculate a_{n+1}^{exp}
- 651 3) Calculate a_{n+1}^{imp} and $u_{n+1} = u_n + \frac{\Delta t}{2} \left(a_n^{exp} + a_{n+1}^{exp}\right) + (\Delta t) a_{n+1}^{imp}$

652 This scheme reduces to the traditional velocity Verlet when a^{imp} is set to zero.
 653 Note that $a_{n+1}^{exp} = a_{n+1}^{exp}(x_{n+1}, t_n)$ is an explicit function of x_{n+1} and other quantities
 654 evaluated at time t_n , while $a_{n+1}^{imp} = a_{n+1}^{imp}(u_{n+1}, x_{n+1}, t_n)$ additionally depends on u_{n+1} ,

and needs to be solved implicitly. For this reason in step three, a_{n+1}^{imp} and u_{n+1} need to be solved simultaneously, as described in the next subsection.

In equation (1), the forces due to ocean drag, atmospheric drag and sea ice drag are treated implicitly. The force due to sea surface slope and wave radiation are treated explicitly. The Coriolis term is handled using Crank-Nicolson scheme so that half of the effect is implicit and half is explicit. The elastic part of the interactive forces is treated explicitly, while the interactive damping is handled semi-implicitly in that the drag force on element A by element B depends on the velocities of elements A and B evaluated at time t_{n+1} and t_n , respectively.

7.2 Solving for the velocity implicitly

Since this modified scheme contains some forcing terms which are handled implicitly, a_{n+1}^{imp} and u_{n+1} need to be calculated simultaneously. We demonstrate how this is done, using a simplified one-dimensional version of equation (1), neglecting the atmospheric drag, sea ice drag and Coriolis force, so that the only implicitly treated term is the ocean drag. In this demonstration, we use a superscript to denote the ocean drag force, F^o , and ocean velocity, u^o , to avoid confusion with the subscripts indicating time step. We also define an explicit force, F^{exp} , which accounts for all forces not proportional the element velocity. With these simplifications, the implicit and explicit accelerations are

$$a^{exp} = \frac{1}{M}(\vec{F}^{exp}) \quad (21)$$

$$a^{imp} = \frac{1}{M}(F^o) \quad (22)$$

The ocean drag force at time t_{n+1} is modeled (mostly) implicitly as

$$F_{n+1}^o = \tilde{c}^o |u_n^o - u_n| (u_n^o - u_{n+1}), \quad (23)$$

where \tilde{c}^o is the effective drag coefficient, accounting for the dimensions of the ice element (see equation 12).

Step 3 of the modified velocity Verlet scheme can be rewritten by introducing an intermediate velocity u^* , which only depends on the velocity and acceleration at time t_n ,

$$u_n^* = u_n + \frac{1}{2}(\Delta t)a_n^{exp}. \quad (24)$$

Using this, the updated velocity (Step 3) can be written

$$u_{n+1} = u_n^* + \frac{\Delta t}{2}a_{n+1}^{exp} + (\Delta t)a_{n+1}^{imp}. \quad (25)$$

Including the forcing terms into this equations gives

$$u_{n+1} = u_n^* + \frac{\Delta t}{2M}(F_{n+1}^{exp}) + \frac{\Delta t}{M} \left(c_w |u_n^o - u_n| (u_n^o - u_{n+1}) \right) \quad (26)$$

Solving for $u(t_{n+1})$ in terms of quantities which only depend on the previous time step gives

$$u_{n+1} = \frac{u_n^* + \frac{\Delta t}{2M}(F_{n+1}^{exp}) + \frac{\Delta t}{M} \left(c_w |u_n^o - u_n| (u_n^o - u_{n+1}) \right)}{\left(1 + \frac{\Delta t}{M} c_w |u_n^o - u_n| \right)} \quad (27)$$

Once the u_{n+1} has been found, it can be used to calculate the explicit and implicit accelerations, which are required for the next time step.

Finally, we note that the the drag term (equation 23) is not entirely implicit, since the element velocity inside the absolute value is evaluated at time t_n , rather than at time t_{n+1} . This is done so that we can solve for the updated velocity analytically. One consequence of this is that it can give rise to a small oscillation in the element velocity. This oscillation is addressed by using a predictive corrective scheme: after solving for a first guess of the velocity at time t_{n+1} , this estimate of the velocity is used to update the estimate of the drag force (i.e.: inside the absolute value signs). This updated drag, can now be used to repeat the process described above to find an improved estimate of the velocity. We found that two iterations were sufficient to remove the unwanted oscillation.

The procedure described in this section is easily extended to include more forcing terms and two dimensions (where it involves inverting a 2×2 matrix).

8 Appendix C

Connecting bonds across processor boundaries

Since the KID is parallelized across multiple processors, it often happens that two elements on different processes are bonded together. Keeping track of numerical bonds across processor boundaries requires a lot of book keeping. In this section we describe the how KID handles bonds across processor boundaries.

The basics of the bond bookkeeping work as follows: consider an element A and an element B that are bonded together. Each element has a copy of the bond (a piece of memory which describes the bond between the two elements), which is stored with the element. Let A-B be the bond stored by element A, and B-A be the bond stored by element B. Bond A-B contains a pointer which points to element B and bond B-A contains a pointer which points to element A.

Consider a situation where element A and B are originally on Processor 1, and then element B moves to Processor 2. When this occurs, the memory assigned to element B on processor 1 is removed, and is allocated on Processor 2. This means that the pointer to element B in bond A-B (stored in element A on Processor 1) is no longer assigned. Similarly, the pointer to element A in bond B-A (stored in element B on Processor 2) is no longer assigned. Before the next time step, a halo update occurs, so that the there is a copy of element A in the halo of Processor 2 and a copy of element B in the halo of Processor 1. After the halo update, the bonds A-B and B-A have to be reconnected on both Processor 1 and 2. To aid in reconnecting the bonds, a copy of the grid cell number of element B is stored in the bond A-B and a copy of the grid cell number of element A is stored in the bond B-A. We refer to this as the ‘most recent address’. Before a bond is moved from one processor to another, the ‘most recent address’ is updated, so that the bond can be reconnected later. To reconnect bond A-B on Processor 1 (for example), we find the most recent address of element B, and search through the list of elements in the grid cell corresponding to the most recent address of element B until element B is found. The pointer to element B in bond A-B is reassigned, and the bond is said to be connected.

The reconnected bond A-B (stored in element A) is said to be working properly when the following four test pass:

1. The pointer to element B is assigned on bond A-B.
2. The corresponding bond B-A exists on element B.
3. A pointer to element A exists in this bond B-A.
4. The element A which is being pointed to is the same element A where you started.

A useful tool for debugging the disconnecting and reconnecting bonds routines is that each element is assigned a unique number so that elements are easily identified.

732 **Acknowledgments**

733 This study is supported by awards NA08OAR4320752 and NA13OAR439 from the Na-
734 tional Oceanic and Atmospheric Administration, U.S. Department of Commerce. Special
735 thanks to Robert Hallberg who contributed to this study through many helpful conversa-
736 tions. The statements, findings, conclusions, and recommendations are those of the authors
737 and do not necessarily reflect the views of the National Oceanic and Atmospheric Admin-
738 istration, or the U.S. Department of Commerce. The simulations in this paper can be re-
739 produced using the model code and experimental setups found at https://github.com/sternalon/Iceberg_repository.

740 References

- 741 Asay-Davis, X. S., S. L. Cornford, B. K. Galton-Fenzi, R. M. Gladstone, G. H. Gud-
 742 mundsson, D. M. Holland, P. R. Holland, and D. F. Martin (2016), Experimental de-
 743 sign for three interrelated marine ice sheet and ocean model intercomparison projects:
 744 MISMIP v. 3 (MISMIP+), ISOMIP v. 2 (ISOMIP+) and MISOMIP v. 1 (MISOMIP1).
 745 *Geoscientific Model Development* 9, no. 7: 2471.
- 746 Arrigo, K. R., G. L. van Dijken, D. G. Ainley, M. A. Fahnestock, and T. Markus (2002).
 747 Ecological impact of a large Antarctic iceberg. *Geophys. Res. Lett.*, 29(7).
- 748 Alley, R. B., H. J. Horgan, I. Joughin, K. M. Cuffey, T. K. Dupont, B. R. Parizek, S.
 749 Anandakrishnan, and J. Bassis (2008), A simple law for ice-shelf calving. *Science* 322,
 750 no. 5906, 1344-1344.
- 751 Bassis, J. N., and S. Jacobs (2013), Diverse calving patterns linked to glacier geometry.
 752 *Nature Geoscience*, 6(10), 833-836.
- 753 Benn, D. I., C. R. Warren, and R. H. Mottram (2007). Calving processes and the dynam-
 754 ics of calving glaciers. *Earth-Science Reviews*, 82(3), 143-179.
- 755 Bigg, G. R., Wadley, M. R., Stevens, D. P., and Johnson, J. A. (1997), Modeling the dy-
 756 namics and thermodynamics of icebergs. *Cold Regions Science and Technology*, 26(2),
 757 113-135.
- 758 Borstad, C. P., A. Khazendar, E. Larour, M. Morlighem, E. Rignot, M. P. Schodlok, and
 759 H. Seroussi (2012), A damage mechanics assessment of the Larsen B ice shelf prior to
 760 collapse: Toward a physically-based calving law, *Geophys. Res. Lett.*, 39, L18502
- 761 Biddle, L. C., J. Kaiser, K. J. Heywood, A. F. Thompson and A. Jenkins (2015), Ocean
 762 glider observations of iceberg-enhanced biological productivity in the northwestern
 763 Weddell Sea, *Geophys. Res. Lett.*, 42, 459-465.
- 764 De Rydt, J., and G. H. Gudmundsson (2016), Coupled ice shelf ocean modeling and com-
 765 plex grounding line retreat from a seabed ridge. *J. of Geophys. Res.: Earth Surface*,
 766 121(5), 865-880.
- 767 Dunne, J.P., J.G. John,, A.J. Adcroft, S.M. Griffies, R.W. Hallberg, E. Shevliakova, R.J.
 768 Stouffer, W. Cooke, K.A. Dunne, M.J Harrison, and J.P. Krasting (2012), GFDL's
 769 ESM2 global coupled climate-carbon Earth System Models. Part I: Physical formula-
 770 tion and baseline simulation characteristics. *J. of Climate*, 25(19), 6646-6665.
- 771 Depoorter, M. A., J. L. Bamber, J. A. Griggs, J. T. M. Lenaerts, Stefan RM Ligtenberg,
 772 M. R. van den Broek, and G. Moholdt (2013), Calving fluxes and basal melt rates of
 773 Antarctic ice shelves. *Nature*, 502(7469), 89-92.
- 774 Determan J., Gerdes R. (1994), Melting and freezing beneath ice shelves: implications
 775 from a three-dimensional ocean-circulation model. *Ann. Glaciol.*, 20, 413-419.
- 776 Dowdeswell, J. A., and J. L. Bamber (2007), Keel depths of modern Antarctic icebergs
 777 and implications for sea-floor scouring in the geological record. *Marine Geology*,
 778 243(1), 120-131.
- 779 Duprat, L. P., G. R. Bigg, and D. J. Wilton (2016), Enhanced Southern Ocean marine pro-
 780 ductivity due to fertilization by giant icebergs. *Nature Geoscience*.
- 781 Eckert, E. R. G. (1950). Introduction to the Transfer of Heat and Mass. McGraw-Hill.
- 782 Fogwill, C.J., E. van Sebille, E.A. Cougnon, C.S. Turney, S.R. Rintoul, B.K. Galton-Fenzi,
 783 G.F. Clark, E.M. Marzinelli, E.B. Rainsley, and L. Carter (2016), Brief communication:
 784 Impacts of a developing polynya off Commonwealth Bay, East Antarctica, triggered by
 785 grounding of iceberg B09B. *The Cryosphere*, 10(6), p.2603.
- 786 Gladstone, R. M., G. R. Bigg, and K. W. Nicholls. (2001), Iceberg trajectory model-
 787 ing and meltwater injection in the Southern Ocean (1978-2012). *J. of Geophys. Res.:*
 788 *Oceans*, 106(C9), 19903-19915.
- 789 Goldberg, D. N., C. M. Little, O. V. Sergienko, A. Gnanadesikan, R. Hallberg, and M.
 790 Oppenheimer (2012), Investigation of land ice/ocean interaction with a fully coupled
 791 ice-ocean model: 1. Model description and behavior. *J. of Geophys. Res.: Earth Surface*,
 792 117(F2).

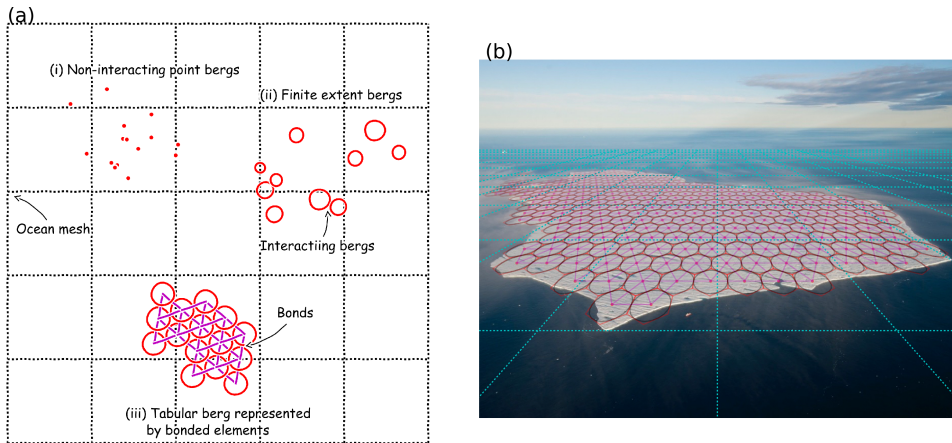
- 793 Gladish, C. V., D. M. Holland, P. R. Holland, and S. F. Price (2012), Ice-shelf basal chan-
794 nels in a coupled ice/ocean model. *J. of Glaciol.*, 58(212), 1227-1244.
- 795 Grosfeld K., R. Gerdes, J. Determan (1997), Thermohaline circulation and interaction
796 between ice shelf cavities and the adjacent open ocean. *J. Phys. Oceanogr.*, **102**, C7,
797 15959-15610.
- 798 Grosfeld, K., and H. SandhŁger, (2004). The evolution of a coupled ice shelfDocean sys-
799 tem under different climate states. *Global and Planetary Change*, 42(1), 107-132.
- 800 Hallberg, R., A. Adcroft, J. P. Dunne, J. P., Krasting, R. J., and Stouffer (2013), Sensitiv-
801 ity of twenty-first-century global-mean steric sea level rise to ocean model formulation.
802 *J. of Climate*, 26(9), 2947-2956.
- 803 Holland D. M., Jenkins A. (2001), Adaptation of an isopycnic coordinate ocean model for
804 the study of circulation beneath ice shelves. *Mon. Wea. Rev.*, 129, 1905-1927.
- 805 Holland P. R. and D. L. Feltham (2006), The effects of rotation and ice shelf topography
806 on frazil-laden Ice Shelf Water plumes. *J. Phys. Oceanogr.*, 36, 2312-2327.
- 807 Holland, D. M., and A. Jenkins (1999), Modeling thermodynamic ice-ocean interactions at
808 the base of an ice shelf. *J. of Phys. Oceanogr.* 29.8, 1787-1800.
- 809 Hellmer H.H., Olbers D. J. (1989), A two-dimensional model for the thermohaline circula-
810 tion under an ice shelf. *Antarctic Science*, 1, 325- 336.
- 811 Henderson J., J. S. P. Loe (2016), The Prospects andChallenges for Arctic Oil Develop-
812 ment. *Oil, Gas and Energy Law Journal (OGEL)*, 14 (2)
- 813 Hopkins, M. A. (1996). On the mesoscale interaction of lead ice and floes. *J. of Geophys.
Res.: Oceans*, 101(C8), 18315-18326.
- 814 Hopkins, M. A. (2004). A discrete element Lagrangian sea ice model. *Engineering Com-
815 putations*, 21(2/3/4), 409-421.
- 816 Gaskill, H. S., and J. Rochester (1984). A new technique for iceberg drift prediction. *Cold
817 Reg. Sci. Technol.*, 8(3), 223-234.
- 818 Jacobs, S. S., H. H. Helmer, C. S. M. Doake, A. Jenkins, R. M. Frolich (1992), Melting
819 of ice shelves and the mass balance of Antarctica. *J. of Glaciol.*, 38(130), 375-387.
- 820 Jakobsen, T. (2001). Advanced character physics. In *Game Developers Conference*, Vol. 3.
- 821 Jenkins, A., P. Dutrieux, S. S. Jacobs, S. D. McPhail, J. R. Perrett, A. T. Webb, and D.
822 White (2010), Observations beneath Pine Island Glacier in West Antarctica and implica-
823 tions for its retreat. *it Nature Geo.*, 3(7), 468-472.
- 824 Jacobs, S. S., A. Jenkins, C. F. Giulivi, and P. Dutrieux (2011). Stronger ocean circulation
825 and increased melting under Pine Island Glacier ice shelf. *Nature Geo.*, 4(8), 519-523.
- 826 Jongma, J. I., E. Driesschaert, T. Fichefet, H. Goosse, and H. Renssen (2009), The ef-
827 fect of dynamic-thermodynamic icebergs on the Southern Ocean climate in a three-
828 dimensional model, *Ocean Modell.*, 26, 104D113.
- 829 Kubat I., M. Sayed, S. Savage, T. Carrières (2005), An operational model of iceberg drift
830 *Int. J. Off. Polar Eng.*, 15 (2), 125D131
- 831 Lewis E.L. and R.G. Perkin (1986), Ice pumps and their rates. *J. of Geophys. Res.*, 91,
832 11756-11762.
- 833 Losch, M. (2008). Modeling ice shelf cavities in a z coordinate ocean general circulation
834 model. *J. of Geophys. Res.: Oceans*, 113(C8).
- 835 Li, B., H. Li, Y. Liu, A. Wang and S. Ji (2014), A modified discrete element model for
836 sea ice dynamics. *Acta Oceanologica Sinica*, 33(1), 56-63.
- 837 Liu, M. B. and G. R. Liu (2010), Smoothed particle hydrodynamics (SPH): an overview
838 and recent developments. *Archives of computational methods in engineering*, 17(1), 25-
839 76.
- 840 Lichéy, C., and H. H. Hellmer (2001). Modeling giant-iceberg drift under the influence of
841 sea ice in the Weddell Sea, Antarctica. *J. of Glaciol.*, 47(158), 452-460.
- 842 Levermann, A., T. Albrecht, R. Winkelmann, M. A. Martin, M. Haseloff, and I. Joughin.
843 (2012), Kinematic first-order calving law implies potential for abrupt ice-shelf retreat.
844 *The Cryosphere*, 6(2), 273-286.

- 846 Mountain, D. G. (1980). On predicting iceberg drift. *Cold Reg. Sci. Technol.*, 1(3-4), 273-
847 282.
- 848 Martin, T., and Adcroft, A. (2010), Parameterizing the fresh-water flux from land ice to
849 ocean with interactive icebergs in a coupled climate model. *Ocean Modelling*, 34(3),
850 111-124.
- 851 Marsh, R., V. O. Ivchenko, N. Skliris, S. Alderson, G. R. Bigg, G. Madec, A. T. Blaker
852 Y. Aksenov, B. Sinha, A.C. Coward, and J.L. Sommer (2015), NEMODICB (v1. 0):
853 interactive icebergs in the NEMO ocean model globally configured at eddy-permitting
854 resolution. *Geoscientific Model Development* 8, no. 5 (2015): 1547-1562.
- 855 MacAyeal D.R. (1984), Thermohaline Circulation Below the Ross Ice Shelf: A Conse-
856 quence of Tidally Induced Vertical Mixing and Basal Melting. *J. Geophys. Res.*, 89,
857 597-606
- 858 Merino, N., Le Sommer, J., Durand, G., Jourdain, N. C., Madec, G., Mathiot, P., and
859 Tournadre, J. (2016), Antarctic icebergs melt over the Southern Ocean: climatology and
860 impact on sea ice. *Ocean Modelling*, 104, 99-110.
- 861 Nicholls K.W. (1996), Temperature variability beneath Ronne Ice Shelf, Antarctica, from
862 thermistor cables. *J. Phys. Oceanogr.*, 11, 1199-1210.
- 863 Nicholls KW, Østerhus S, Makinson K (2009), Ice-Ocean processes over the continental
864 shelf of the southern Weddell Sea, Antarctica: a review. *Rev. Geophys.* 47(3).
- 865 Omelyan, I. P., M. I. Mryglod, and R. Folk (2002), Optimized Verlet-like algorithms for
866 molecular dynamics simulations. *Physical Review E*, 65(5), 056706.
- 867 Pizzolato, L., S. E. Howell, C. Derksen, J. Dawson, L. Copland (2014), Changing sea ice
868 conditions and marine transportation activity in Canadian Arctic waters between 1990
869 and 2012, *Climatic Change* 123 (2), 161173.
- 870 Pan, W., A. M. Tartakovsky, and J. J. Monaghan (2013). Smoothed particle hydrodynam-
871 ics non-Newtonian model for ice-sheet and ice-shelf dynamics. *J. of Comp. Phys.*, 242,
872 828-842.
- 873 Pralong, A., and M. Funk (2005), Dynamic damage model of crevasse opening and appli-
874 cation to glacier calving, *J. Geophys. Res.*, 110, B01309.
- 875 Rabatel, M., S. LabbÓ and J. Weiss (2015), Dynamics of an assembly of rigid ice floes. *J.*
876 *of Geophys. Res.: Oceans*, 120(9), 5887-5909.
- 877 Rackow, T., C. Wesche, R. Timmermann, H. H. Hellmer, S. Juricke and T. Jung (2017), A
878 simulation of small to giant Antarctic iceberg evolution: differential impact on climatol-
879 ogy estimates. *J. of Geophys. Res.: Oceans*, doi: 10.1002/2016JC012513
- 880 Rignot, E., S. Jacobs, J. Mouginot, and B. Scheuchl (2013), Ice-shelf melting around
881 Antarctica. *Science*, 341, no. 6143 (2013): 266-270.
- 882 Robinson, N. J., M. J. M. Williams, P. J. Barrett, and A. R. Pyne (2010), Observations of
883 flow and ice-ocean interaction beneath the McMurdo Ice Shelf, Antarctica, *J. Geophys.*
884 *Res.*, 115, C03025
- 885 Sergienko, O. V. (2013). Basal channels on ice shelves. *J. of Geophys. Res.: Earth Surface*,
886 118(3), 1342-1355.
- 887 Silva, T. A. M., Bigg, G. R., and Nicholls, K. W. (2006), Contribution of giant icebergs to
888 the Southern Ocean freshwater flux. *J. of Geophys. Res.: Oceans*, 111(C3).
- 889 Smith, K., B. Robison, J. Helly, R. Kaufmann, H. Ruhl, H., T. Shaw, and M. Vernet
890 (2007), Free-drifting icebergs: Hotspots of chemical and biological enrichment in the
891 Weddell Sea, *Science*, 317, 478-482.
- 892 Shepherd, A., and D. Wingham (2007). Recent sea-level contributions of the Antarctic and
893 Greenland ice sheets. *Science*, 315(5818), 1529-1532.
- 894 Stern, A., D. M. Holland, P. R. Holland, A. Jenkins and J. Sommeria (2014), The effect of
895 geometry on ice shelf ocean cavity ventilation: a laboratory experiment. *Experiments in*
896 *Fluids*, 55(5), 1-19.
- 897 Stern, A., Johnson, E., Holland, D.M., Wagner, T.J., Wadhams, P., Bates, R., Abrahamsen,
898 E.P., Nicholls, K.W., Crawford, A., Gagnon, J. and Tremblay, J.E. (2015), Wind-driven
899 upwelling around grounded tabular icebergs. *J. of Geophys. Res.: Oceans*, 120(8), 5820-

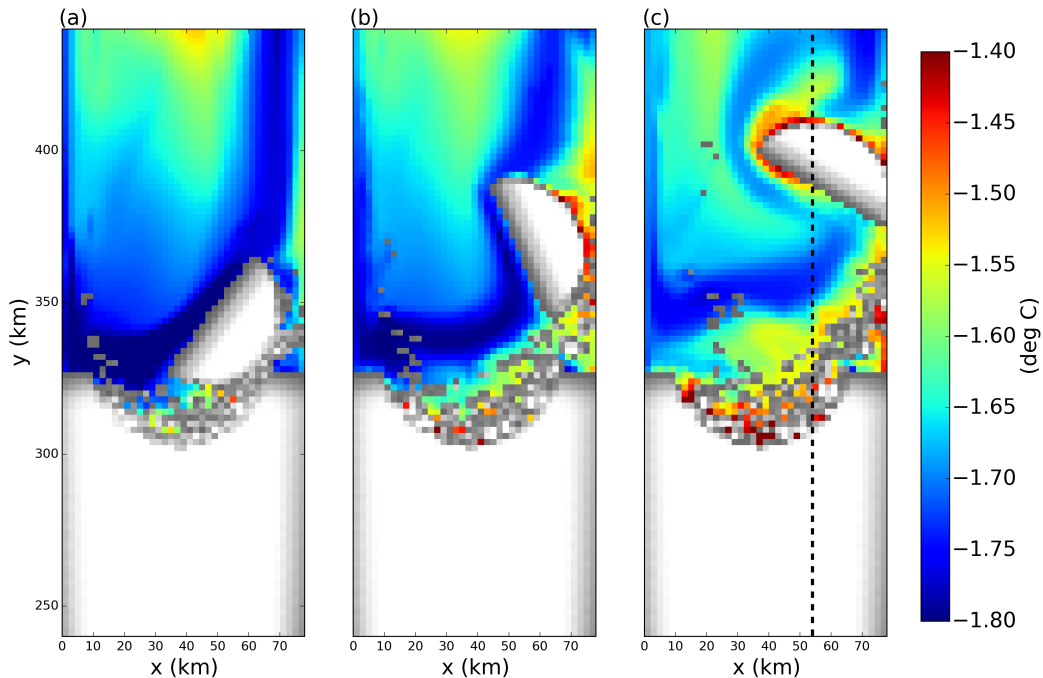
- 900 5835.
- 901 Stern, A., A. Adcroft, and O. Sergienko (2016), The effects of Antarctic iceberg calving
902 size distribution in a global climate model. *J. of Geophys. Res.: Oceans*, 121(8), 5773-
903 5788.
- 904 Swope, W. C., H. C. Andersen, P. H. Berens, and K. R. Wilson (1982), A computer sim-
905 ulation method for the calculation of equilibrium constants for the formation of physi-
906 cal clusters of molecules: Application to small water clusters. *The Journal of Chemical*
907 *Physics* 76, no. 1, 637-649.
- 908 Tournadre, J., N. Bouhier, F. Girard-Ardhuin, and F. RÓmy (2016), Antarctic icebergs dis-
909 tributions 1992-2014. *J. Geophys Res: Oceans*.
- 910 Turnbull I.D., N. Fournier, M. Stolwijk, T. Fosnaes, D. McGonigal (2015), Operational
911 iceberg drift forecasting in Northwest Greenland, *Cold Reg. Sci. Technol.* 110, 1-18
- 912 Unger, J. D., 2014. Regulating the Arctic Gold Rush: Recommended Regulatory Reforms
913 to Protect Alaska's Arctic Environment from Offshore Oil Drilling Pollution . *Alaska L.*
914 *Rev*, 31
- 915 Vernet, M., et al. (2012), Islands of ice: Influence of free-drifting Antarctic icebergs on
916 pelagic marine ecosystems, *Oceanography*, 25(3), 38-39
- 917 Wagner, T. J., Wadhams, P., Bates, R., Elosegui, P., Stern, A., Vella, D., E. P. Abraham-
918 sen, A. Crawford, and Nicholls, K. W. (2014), The ÒfootlooseÓ mechanism: Iceberg
919 decay from hydrostatic stresses. *Geophys. Res. Lett.*, 41(15), 5522-5529.
- 920 Weeks, W. F., and W. J. Campbell (1973). Icebergs as a fresh-water source: an appraisal.
921 *J. of Glaciol.*, 12(65), 207-233.
- 922 White, L., A. Adcroft, and R. Hallberg (2009), High-order regridding-remapping schemes
923 for continuous isopycnal and generalized coordinates in ocean models. *J. of Comp.*
924 *Phys.*, 228(23), 8665-8692.

Parameter	Symbol	Value	Unit
Domain Length	L_x	80	km
Domain Width	L_y	480	km
Horizontal Resolution	Δx	2	km
Number of vertical layers	N_l	72	non-dim
Horizontal Viscosity	ν_H	6.0	$m^2 s^{-1}$
Diapycnal Viscosity	ν_V	10^{-3}	$m^2 s^{-1}$
Horizontal Diffusivity	ϵ_H	1.0	$m^2 s^{-1}$
Diapycnal Diffusivity	ϵ_V	5×10^{-5}	$m^2 s^{-1}$
Initial Surface Temperature	T_t	-1.9	$^{\circ}C$
Initial Bottom Temperature	T_b	1.0	$^{\circ}C$
Initial Surface Salinity	S_t	33.8	psu
Initial Bottom Salinity	S_b	34.7	psu
Maximum Ocean depth	H_{ocean}	720	m
Relaxation Time of Sponge Layer	T_{sponge}	0.1	days
Length of Sponge Layer	L_{sponge}	10	km
KID Time Step	dt	10	s
Elastic interactive force spring constant	κ_e	10^{-5}	$kg s^{-2}$

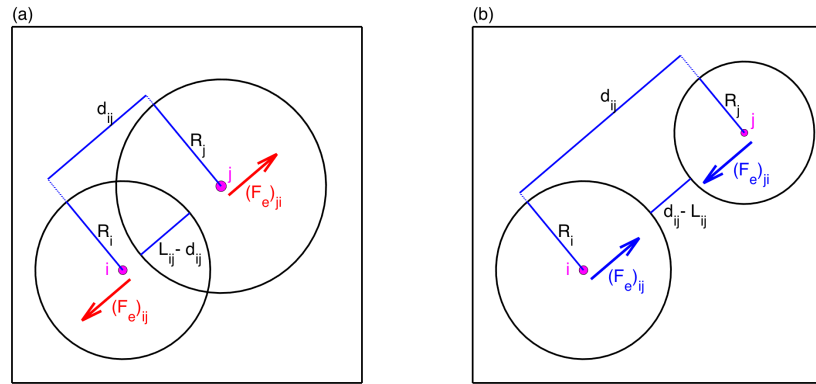
925 **Table 1.** Parameters used in the model. The ocean model parameters are as described in Asay-Davis et al
 926 [2016]



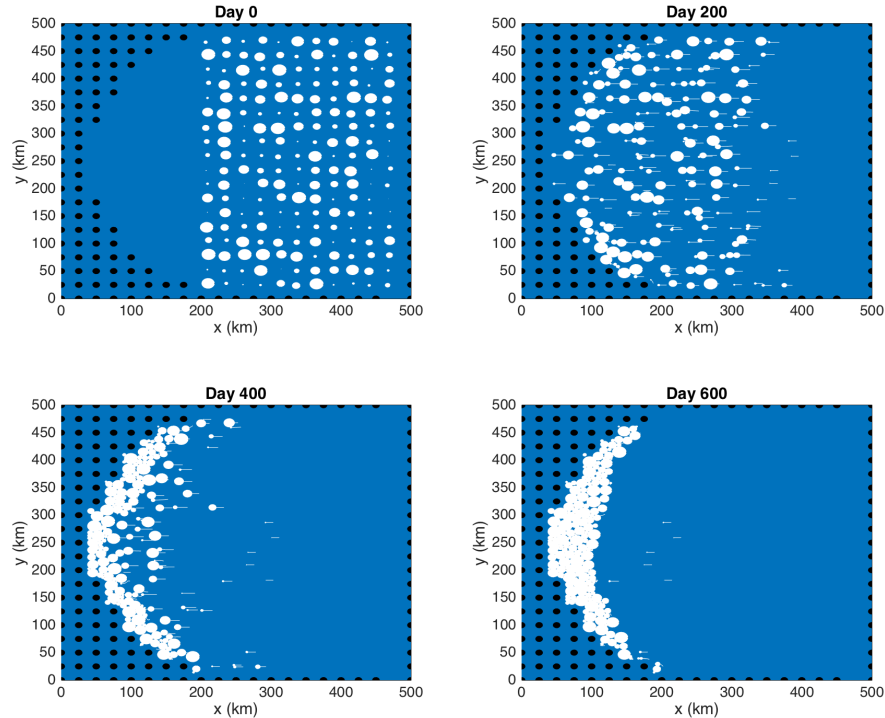
927 **Figure 1.** Schematic showing how tabular icebergs are constructed using Lagrangian elements. (a) Hierar-
928 chy of ice elements' physical structure: (i) Previous icebergs models represent icebergs using non-interacting
929 point-particle elements; (ii) In the KID ice elements are given finite extent so that they are able to interact
930 with the ocean across multiple grid cells, and can interact with other elements; (iii) These finite extent el-
931 ements can be join together by numerical bonds (magenta lines) to form larger structures such as tabular
932 icebergs. (b) Areal photograph of a tabular iceberg with elements superimposed over it to illustrate how
933 the Lagrangian elements can be used to model tabular icebergs. In this schematic the ice elements (purple
934 dots) are initialized in a staggered lattice covering the surface area of the iceberg. For purposes of mass ag-
935 gregation, the ice elements are assumed to have hexagonal shape (red hexagons). For purposes of element
936 interactions, the ice elements are assumed to be circular (black circles). Elements are initially bonded to adja-
937 cent elements using numerical bonds (magenta lines). These numerical bonds form equilateral triangles which
938 give the shape rigidity. An ocean grid has been included (dashed cyan lines).The background photo is an areal
939 photograph of iceberg PIIB (Area= 42 km²) taken in Baffin Bay in 2012. A red ship can be identified on the
940 bottom of the photo for scale.



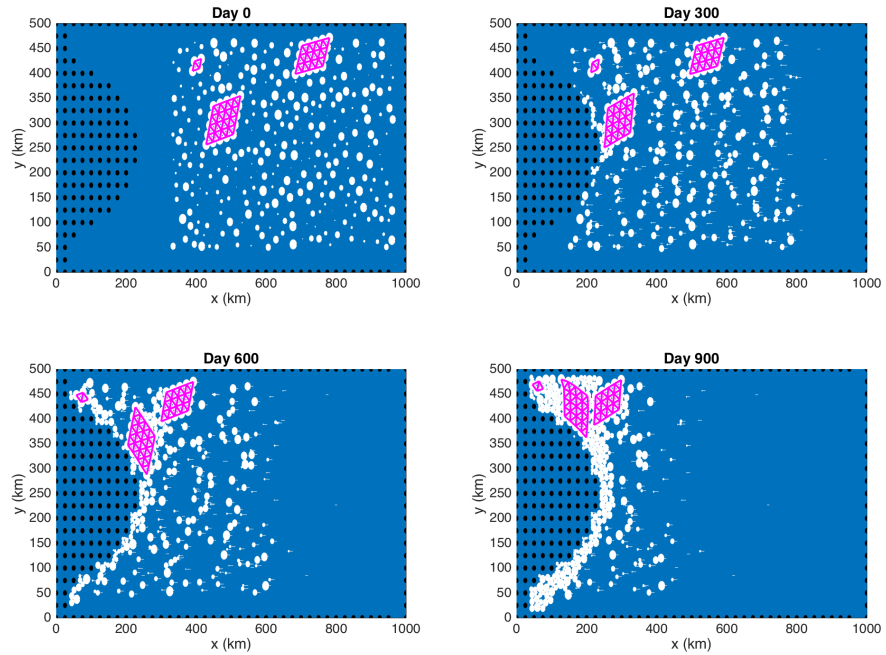
941 **Figure 2.** Snapshots of the sea surface temperature in the KID tabular iceberg calving simulation. Snap-
942 shots are taken (a) 7, (b) 15, and (c) 30 days after calving. Grid cells with ice mass $> 10^4$ kg are plotted in
943 white, with grey shading indicating thinner ice. The dashed line in panel (c) shows the location of the vertical
944 transects shown in Figures 8 and 11.



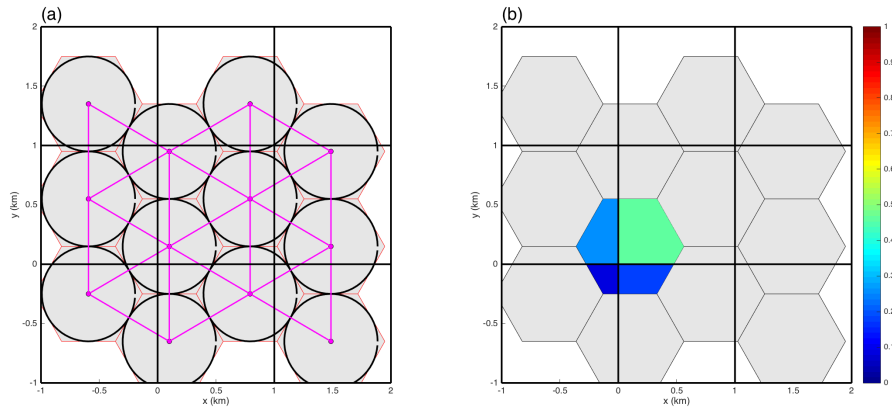
945 **Figure 3.** Diagram showing the (a) repulsive and (b) attractive elastic interactive forces between two ele-
 946 ments, i and j . R_i and R_j are the interactive radii of element i and j , respectively. d_{ij} is the distance between
 947 the centers of elements. $L_{i,j} = R_i + R_j$ is the critical-interaction-length scale. $(F_e)_{ij}$ and $(F_e)_{ji}$ are the elastic
 948 forces applied to elements i and j , respectively (equation 7). A frictional damping force is also applied, which
 949 opposes the relative velocity of the elements (not shown). The attractive forces are only applied when the two
 950 elements are bonded together (i.e.: $B_{ij} = 1$).



951 **Figure 4.** Results of an ice-only KID simulation with no bonds between ice elements. Ice elements are
 952 initialized throughout the domain, as shown in top left panel. The elements are forced by an imposed west-
 953 ward ocean current of $u=0.1\text{m/s}$ (no ocean model is used). Forces due to sea surface slope, atmospheric drag,
 954 Coriolis and sea ice drag are set to zero. The figure shows snapshots of ice element positions at time $t=0, 200,$
 955 400 and 600 days. The size of the dots shows the surface area (and interaction radius) of each ice element.
 956 The white tails behind the elements show the elements' positions over the preceding two days. Land points
 957 are shown by black circles.

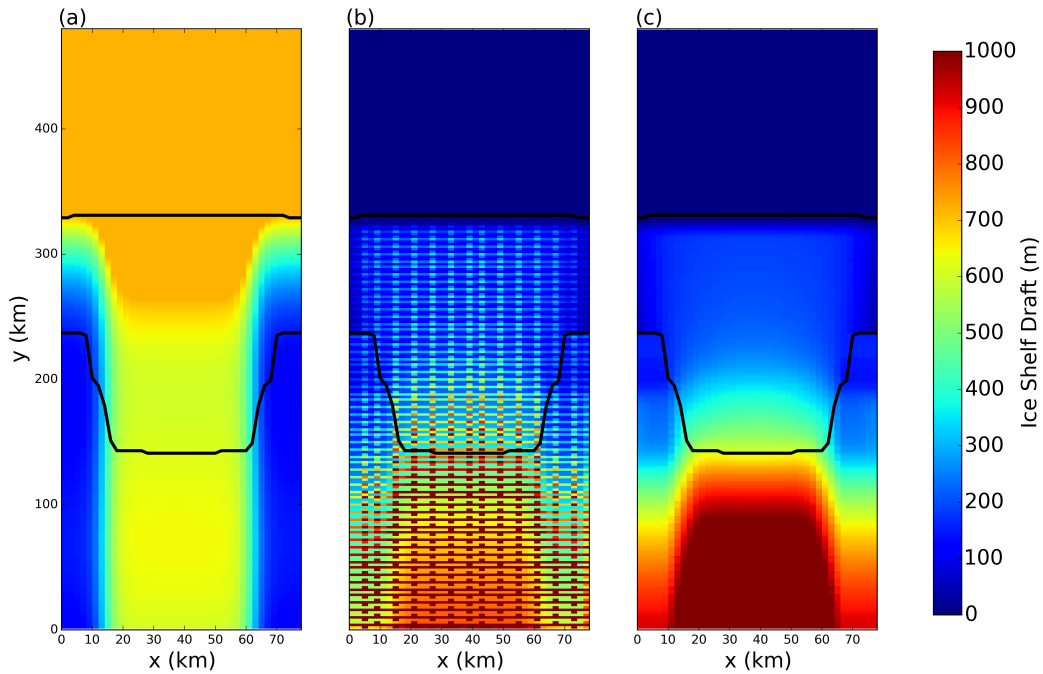


958 **Figure 5.** Results of an ice-only KID simulation using bonds between elements. Ice elements are initialized
 959 throughout the domain, as shown in top left panel. Three tabular icebergs are included, with 25, 16 and 4
 960 elements respectively. The elements are forced by an imposed westward ocean current of $u=0.1\text{m/s}$ (no ocean
 961 model is used). Forces due to sea surface slope, atmospheric drag, Coriolis and sea ice drag are set to zero.
 962 The figure shows snapshots of ice element positions at time $t=0, 300, 600$, and 900 days. The size of the dots
 963 shows the surface area (and interaction radius) of each ice element. The white tails behind the elements show
 964 the elements' positions over the preceding two days. Bonds between ice elements are plotted in magenta.
 965 Land points are shown by black circles.

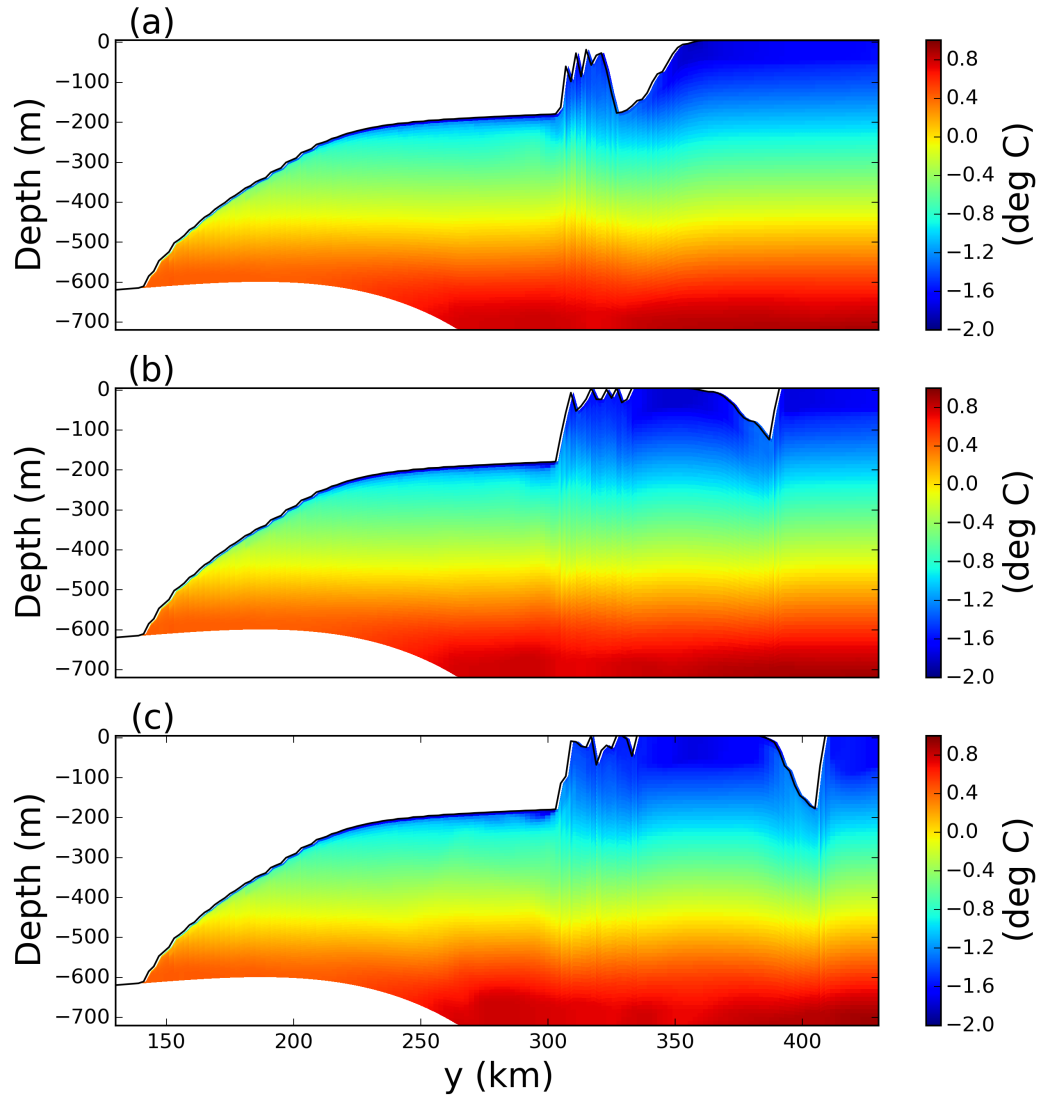


966 **Figure 6.** (a) Ice element packing and geometry: ice elements (purple dots) are initialized in a stag-
967 gered lattice. For purposes of mass aggregation, the ice elements are assumed to have hexagonal shape (red
968 hexagons). For purposes of element interactions, the ice elements are assumed to be circular (black circles). (b) Intersections of
969 an hexagonal element and the ocean grid. The colors indicate the fraction of the hexagon that lies in each grid
970 cell. These fractions are used as weights to spread KID properties to the ocean grid (see text for more details).
971

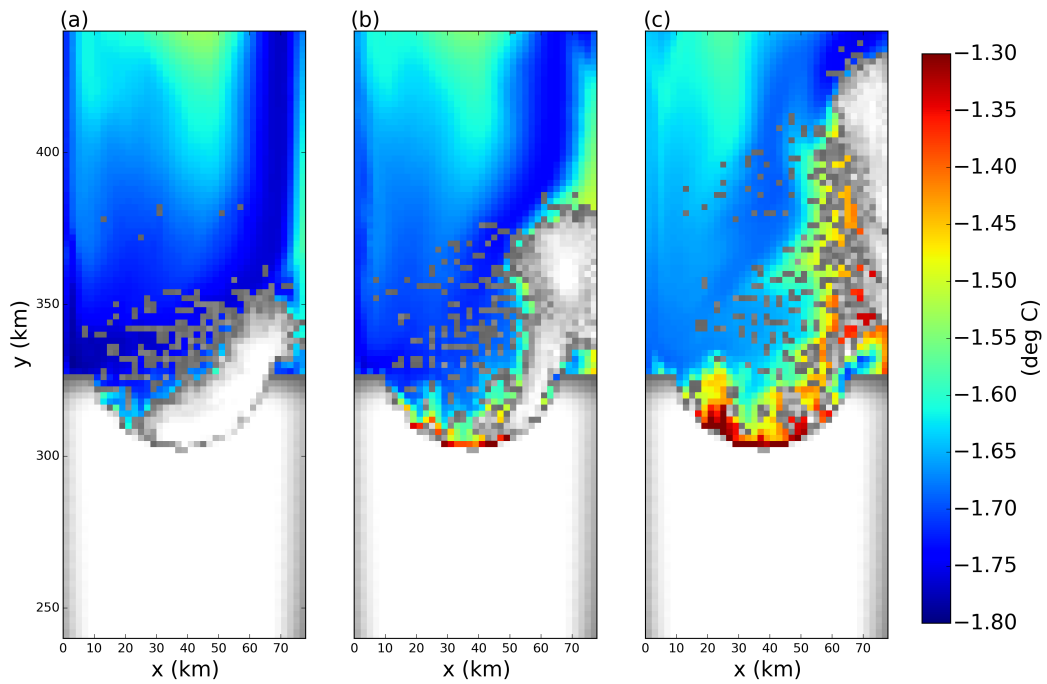
972



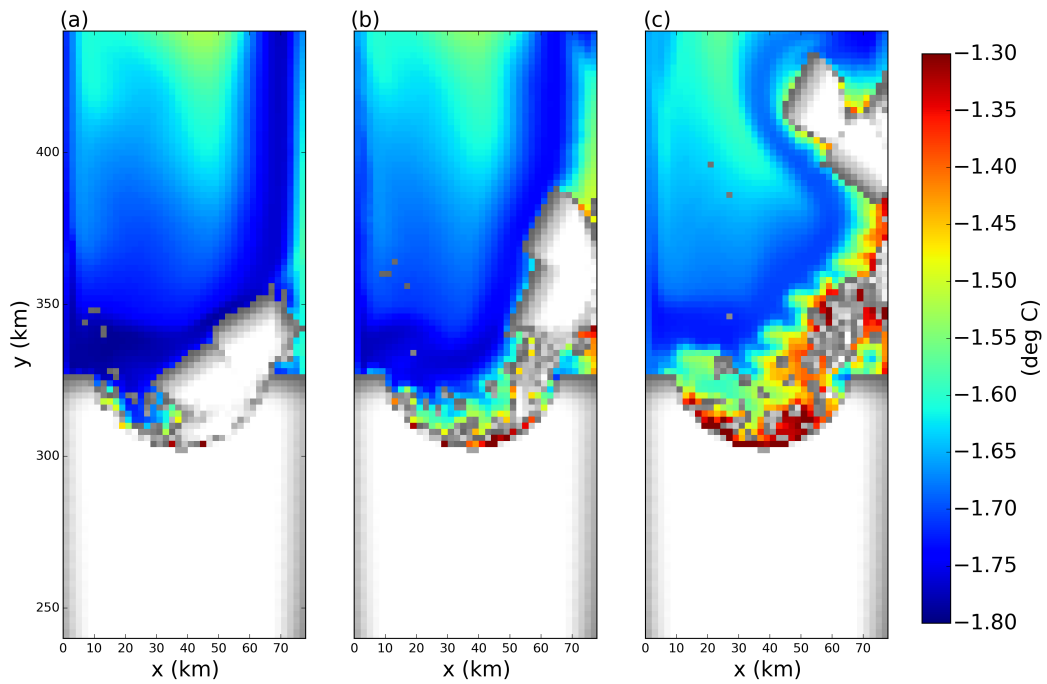
973 **Figure 7.** (a) Ocean bottom topography and (c) ice-shelf draft used to initialized the tabular iceberg calv-
974 ing simulation. The ice draft is calculated from the total mass in an ocean grid cell after the mass-spreading
975 interpolation has been applied (as explained in Section 2.3). Panel (b) shows the initial ice draft that would be
976 calculated if the mass-spreading interpolation were not used (i.e. elements treated as point masses).



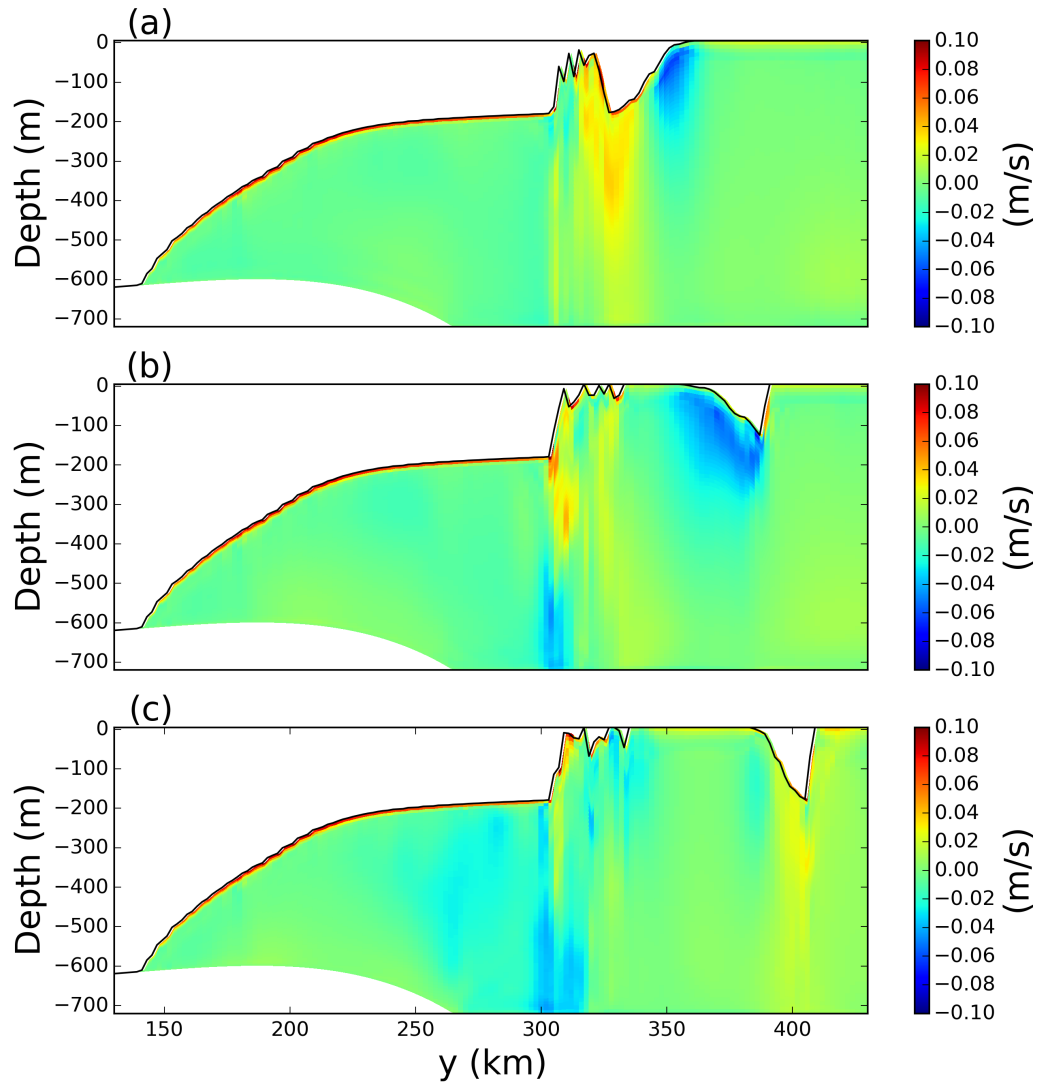
977 **Figure 8.** Snapshots of vertical sections of ocean temperature at $x=54$ km in the tabular-iceberg-calving
 978 Control experiment. Snapshots are taken (a) 7, (b) 15, and (c) 30 days after calving. The position of the
 979 vertical transects is shown by the dashed lines in Figure 2c.



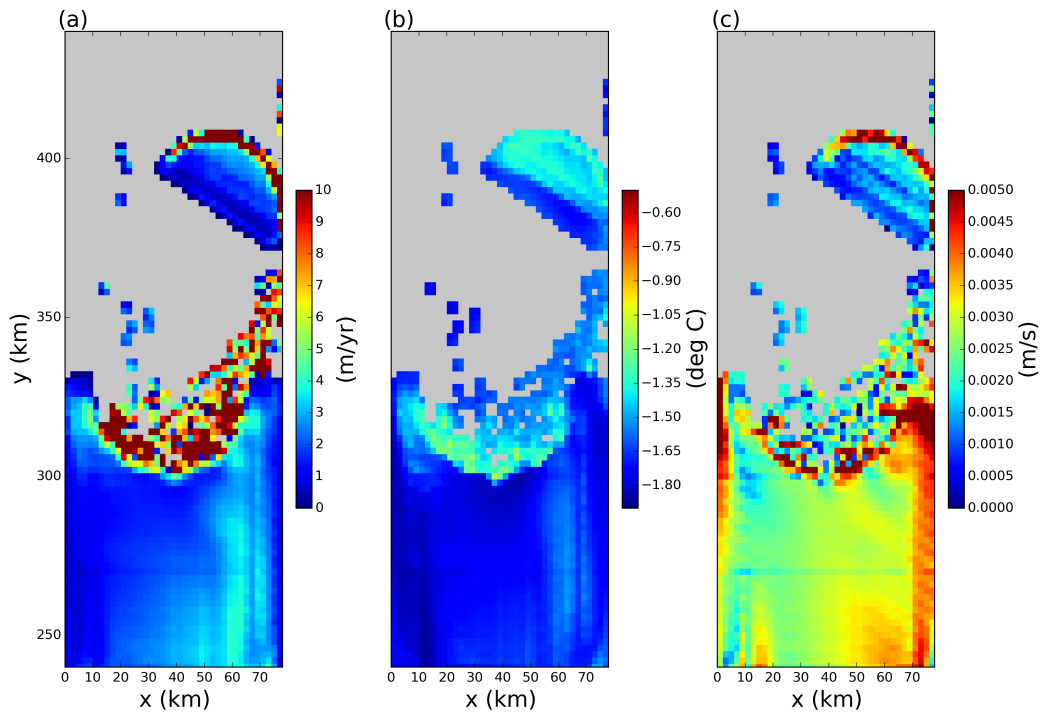
980 **Figure 9.** No bonds simulation: Snapshots of the sea surface temperature for a simulation where all bonds
981 have been broken. Snapshots are taken (a) 7, (b) 15, and (c) 30 days after calving. Grid cells with ice mass >
982 10^4 kg are plotted in white, with grey shading indicating thinner ice.



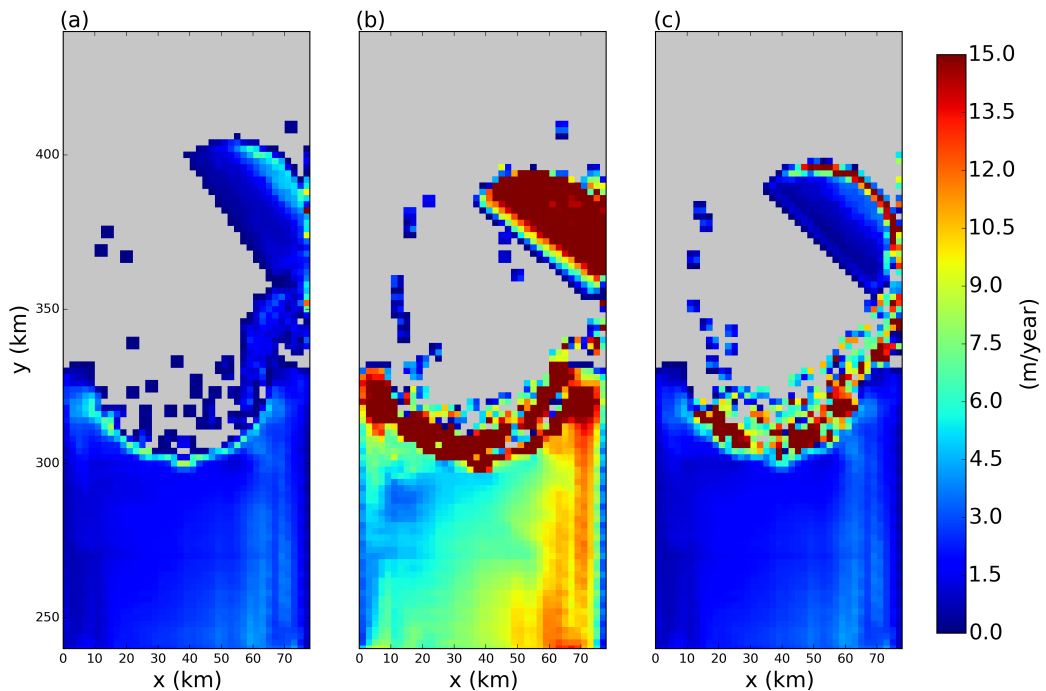
983 **Figure 10.** Iceberg splitting simulation: Snapshots of the sea surface temperature for the iceberg splitting
984 simulation. Snapshots are taken (a) 7, (b) 15, and (c) 30 days after calving. Grid cells with ice mass $> 10^4$ kg
985 are plotted in white, with grey shading indicating thinner ice.



986 **Figure 11.** Snapshots of vertical sections of meridional velocity at $x=54$ km in the tabular-iceberg-calving
 987 Control experiment. Snapshots are taken (a) 7, (b) 15, and (c) 30 days after calving. The position of the
 988 transects is shown by the dashed line in Figure 2c.



989 **Figure 12.** Results of the tabular-iceberg-calving experiment 30 days after the iceberg calves. The three
 990 panels show snapshots of the (a) melt rate, (b) top-of-ocean temperature and (c) u^* at the base of the ice shelf.
 991 Ocean grid cells without ice are masked out in grey.



992 **Figure 13.** Results of the tabular-iceberg-calving experiment using three different melt-rate parametra-
993 tion. Panels show snapshots of the melt rate 30 days after calving for simulations using the (a) three-equation
994 melt-rate parametrization, (b) icebergs-drift melt-rate parametrization, (c) mixed-melt-rate parametrization (as
995 described in Section 2.5.). Ocean grid cells without ice are masked out in grey.

996 **9 Supplementary Material 1**

997 The experiment configuration used to initialize the calving-tabular-iceberg simulation
998 (in this study) is the same as that of the Ocean0 setup in the MISOMIP, with the follow-
999 ing three changes made:

- 1000 1. The ‘calving criteria’ used in the MISOMIP study (which states that all points in
1001 the ice shelf with thickness less than 100m are set to zero thickness) has not been
1002 used.
- 1003 2. The ice shelf has been thickened on the flanks of the domain, so that the latitude of
1004 the grounding line increases away from the center of the ice shelf.
- 1005 3. The ice shelf is configured to be symmetric about its meridional center line ($x =$
1006 $\frac{L_x}{2}$). This was achieved by using the average of the left and right flanks of the ice-
1007 shelf thickness.

1008 These three changes were made in order to make the circulation beneath the ice shelf eas-
1009 ier to interpret.